2012

Theoretical studies of the interaction of excitons with charged impurities in single-walled carbon nanotubes

Benjamin Obi Tayo
Lehigh University

Theoretical Studies of the Interaction of Excitons with Charged Impurities in Single-Walled Carbon Nanotubes

by

Benjamin O. Tayo

A Dissertation
Presented to the Graduate Committee
of Lehigh University
in Candidacy for the Degree of
Doctor of Philosophy
in
Physics

Lehigh University
September 2012

Approved and recommended for acceptance as a dissertation in partial fulfillment of the requirements for the degree of Doctor of Philosophy.

Benjamin O. Tayo
Theoretical Studies of the Interaction of Excitons with Charged Impurities in Single-Walled Carbon Nanotubes

---

Defense Date

Slava V. Rotkin, Dissertation Director, Chair

Accepted Date

Committee Members

Volkmar Dierolf

Ivan Biaggio

Nelson Tansu

Dimitrios Vavylonis

Acknowledgement

I wish to express my heartfelt gratitude to my thesis advisor Prof. Slava V. Rotkin, whose patient and insightful guidance during the course of this work is deeply appreciated. Many thanks to the professors (V. Dierolf, I. Biaggio, N. Tansu and D. Vavylonis) who served in my dissertation committee for the numerous and useful suggestions they provided and for being very cooperative. I would like to thank the entire physics faculty and staff for making my stay at Lehigh successful. In particular, I express my gratitude to Prof. J. Gunton, Prof. J. Huennekens and Prof. W. Fowler. I also thank Lois and Pam for their kind support. Many people contributed in one way or the other to this work, thanks to Andrei Nemilentsau, Tetyana Ignatova, James Doko, Eric Takor, Obed Nkealah, Brilian Nkealah, Delphine Nkongho, Jones Takor, Gaius Takor, Ruth Dikong, Kadmiel Dikong, Hadassah Dikong, Keturah Dikong, Salome Dikong, Andrew Obi, David Obi, Japheth Obi, Debora Obi, Kaitlyn Rodriguez, Carole Pefung, Gustav Atengong, Mauricio A. Valencia and Elvis Takor. I am recording my indebtedness to Dr. A. M. Dikande for inspiring me to choose the field of theoretical condensed matter physics and for being my scientific father.

Contents

List of Tables

List of Figures

Abstract

A fundamental theory of the electronic and optical properties of semiconductors shows the importance of impurities, which are often unavoidable and can alter intrinsic properties of semiconductor materials substantially. While the subject of impurity doping is well understood in bulk semiconductors, the role and impact of doping in low dimensional materials like carbon nanotubes is still under investigation and there exists significant debate on the exact nature of electronic impurity levels in single-walled carbon nanotubes associated with adatoms. In this work, we address the role of impurities in single-walled carbon nanotubes. A simple model is developed for studying the interaction of bright (singlet) excitons in semiconducting single-wall nanotubes with charged impurities. The model reveals a red shift in the energy of excitonic states in the presence of an impurity, thus indicating binding of excitons in the impurity potential well. Signatures of several bound states were found in the absorption spectrum below the onset of excitonic optical transitions in the bare nanotube. The dependence of the binding energy on the model parameters, such as impurity charge and position, was determined and analytical fits were derived for a number of tubes of different diameter. The nanotube family splitting is seen in the diameter dependence, gradually decreasing with the diameter. By calculating the partial absorption coefficient for a small segment of nanotube the local nature of the wave function of the bound states was derived. Our studies provide useful insights into the role of the physical environment (here, a charged impurity atom) in the manipulation of the excited states of carbon nanotubes. We performed very detailed calculations of the electronic and optical properties of carbon nanotubes in the presence of an immobile impurity atom, thus going beyond previous many-body perturbation theory (MBPT) studies in which the carbon nanotubes were considered in vacuum. This work elucidates the role of impurities in low dimensional semiconductors and provides further insights into the uniqueness of the electronic and optical properties of carbon nanotubes which are viable candidates for the next generation nanoscale optoelectronics applications.

Chapter 1

Introduction

Single-wall nanotubes (SWNTs), tiny hollow cylinders of rolled up graphene sheets, are quasi-one-dimensional (quasi-1D) structures, since their diameter, in the range of one nanometer, is much smaller than the length, up to several hundreds micrometers [1, 2]. Carbon nanotubes were discovered and first characterized in 1991 by Iijima from NEC laboratories (Japan) [3]. This discovery was made possible thanks to the use of state-of-the-art transmission microscopy. The first nanotubes discovered were made of several concentric cylindrical-like shells regularly spaced by an amount of about 3.4 Å as in conventional graphite materials. These multiwall nanotubes (MWNTs) were first synthesized with diameters ranging from a few nanometers to several hundred nanometers for the inner and outer shells, respectively. As for the length, MWNTs extending over several microns are currently synthesized.

Shortly after the discovery of multiwall carbon nanotubes, single-wall carbon nanotubes (SWNTs) were synthesized in abundance using arc-discharge methods with transition-metal catalysts [4, 5]. A carbon nanotube made of a single graphite layer (the graphene sheet) rolled up into a hollow cylinder is called a single-wall nanotube. These tubes have quite small and uniform diameter, of the order of 1 nm $=10^{-9}$ m. Because of the small diameter of a carbon nanotube ($\sim$ 1 nm) and the large length-to-diameter ratio ($> 10^4$), carbon nanotubes are an important system for studying one-dimensional physics.

The discovery of SWNTs came after the popularity of buckyballs, another allotrope of carbon with sixty atoms of carbon in a shell like a soccer ball. More recently, graphene (single sheets of graphite) has been intensively studied. It was isolated from graphite [6, 7] just a few years ago and this opened up a large field of research for 2D atomic crystals. Graphene has unique electronic properties, such as high mobility and interesting pseudo-relativistic physics which can be observed for normal nonrelativistic velocities of charge carriers, making it attractive for both its potential applications and its fundamental physics. SWNTs have the structure of graphene, a honeycomb network of carbon atoms one atom thick, rolled up into a seamless cylindrical tube. The electronic properties of SWNTs can be inferred from graphene by means of the zone folding scheme. Unlike graphene which is a zero band gap semiconductor, SWNTs can either be metallic or gapped semiconductors depending on their chirality (orientation of the graphene lattice). Metallic nanotubes have room temperature conductivities as good as or better than the best metals, and some semiconducting tubes have mobilities higher than mobilities of silicon MOSFETs [8].

SWNTs represent one of the best known materials for the study of 1D physics, both from a theoretical and experimental viewpoint. The 1D nature of SWNTs allows efficient and simple theoretical modeling. Furthermore, an increase in the strength of Coulomb interaction (many-body effects) is observed in SWNTs . The optical transition energies in SWNTs are sensitive to these Coulomb effects have been studied in detail through fluorescence and Raman spectroscopy experiments [9–11]. Although some aspects of the experiments can be interpreted within the context of a simple, noninteracting electron model [12, 13], it has become increasingly clear that Coulomb interactions also play an important role in determining the optical transition energies. Thus Coulomb interaction, enhanced in 1D, determines their electronic and optical properties. The Coulomb interactions (many-body effects) in SWNTs lead to band gap renormalization [14] and formation of strongly correlated electron-hole pairs, i.e., excitons, [15–17] with binding energies of the order of several hundred meV, much greater than in typical bulk (3D) semiconductors.

Solid understanding of the optical properties of SWNTs may allow multiple applications in nanoscale electronics and nanophotonics, making them viable candidates for next-generation nanoscale optoelectronics [18–23].

Both theoretical calculations and experimental measurements confirm that the optical properties of SWNTs are dominated by excitonic effects. Different theoretical approaches have been used to investigate excitons in SWNTs, including the variational solution [24], or Bloch equation (BE) method combined with the tight-binding approximation (TBA) for nanotube single-electron band structure [16]. The most precision was achieved within *ab initio* approach combining the solution of the Bethe-Salpeter (BS) equation with DFT GW-correlated quasiparticle energies [25–28]. The crucial role of excitons for SWNT absorption was confirmed in two-photon experiments in 2005 [29, 30]. Since then the experimental studies on excitons were extensive [31–35]. Various excitonic interactions, such as exciton-phonon coupling [36, 37], exciton-plasmon coupling [38], interaction with external electric and magnetic fields [39, 40] have also been investigated.

Most recently the focus of research was on the interactions of excitons with a single charge of mobile (or localized) electron/hole (thus forming a mobile or localized three-body trion) and exciton interactions with a point charge impurity ions [41–44]. A fundamental theory of the electronic and optical properties of semiconductors shows the importance of impurities, which are often unavoidable and can alter intrinsic properties of semiconductor materials substantially. The single-layer structure of SWNTs makes them extremely sensitive to the surrounding conditions and provides a route for doping such as adsorption of molecules with high electron affinity and this can produce drastic changes in their optical properties [45–48]. While the subject of impurity doping is well understood in bulk semiconductors, the role and impact of doping in low dimensional materials like carbon nanotubes is still under investigation and there exists significant debate on the exact nature of electronic impurity levels in single-walled carbon nanotubes associated with adatoms.

In this thesis, we present a model for the interaction of excitons with an immobile charge impurity adsorbed on a semiconducting SWNT. We demonstrate that this interaction can induce exciton localization in SWNTs. We show that for a given

SWNT, the degree of localization, as indicated by the red shift of the excitonic energy level in a local vicinity of the impurity, depends on the effective charge (effective valency) of the impurity ion, $Z|e|$, and the distance between the ion and SWNT, d. Corresponding scaling laws with Z and d will be derived. Moreover, we discuss the relevance of our approach for the theoretical computation of the absorption spectra of carbon nanotubes in the presence of impurities.

The model can be applied to SWNT interacting with charged molecules/atoms adsorbed on its surface [49, 50], to nanotube-lanthanide ion complexes in solutions [51]. It is known that the ssDNA-wrapped tubes carry a significant surface charge [52–54] due to ionization of the DNA backbone. Thus the model can be relevant for interpretation of the optical shift of the excitonic frequency for the SWNTs coated with DNA [55] (or other ionic polymer [56] or surfactant [57]), the effect formerly attributed to unspecified solvatochromism [58–61]. We speculate that the model can be also applicable to SWNTs placed on a silica substrate, as in the vast majority of optoelectronic devices, because of significant density of the surface states, readily ionized under ambient conditions. The model should also apply to some cases of SWNT chemical functionalization. For example, divalent covalent bonding was shown to preserve original pi-band structure of the SWNT while adding charge groups placed very close to its surface [62].

Thesis outline

This thesis is organized as follows:

- In Chapter 2, we review the basic properties of carbon nanotubes. It begins with a discussion of carbon nanotube structure and basic concepts, followed by electronic properties, including tight-binding approximation (TBA).

- In Chapter 3, we discuss the importance of Coulomb interactions (many-body effects) in the electronic and optical properties of quasi-1D materials like SWNTs. We describe how incorporation of Coulomb interactions into the TBA leads to significant renormalization of the single-particle band structure. Subsequently, we review the BS theory of excitons in SWNTs.

- In Chapter 4, we formulate the theory of interaction of exciton with charged impurities in semiconducting SWNTs. Moreover, we discuss the numerical solution of the impurity scattering equation for excitons. Subsequently, we present results of the impurity binding energy as a function of model parameters.

- In Chapter 5, we discuss optical properties of doped SWNTs. We calculate the absorption spectra of SWNTs in the presence of a single impurity and found new features in the absorption spectra (red shifts of the absorption onset), which we attribute to impurity-induced exciton localized states.

The flowchart below represents a summary of the stages involved in computing the optical spectra of SWNTs in the presence of a single charged impurity.

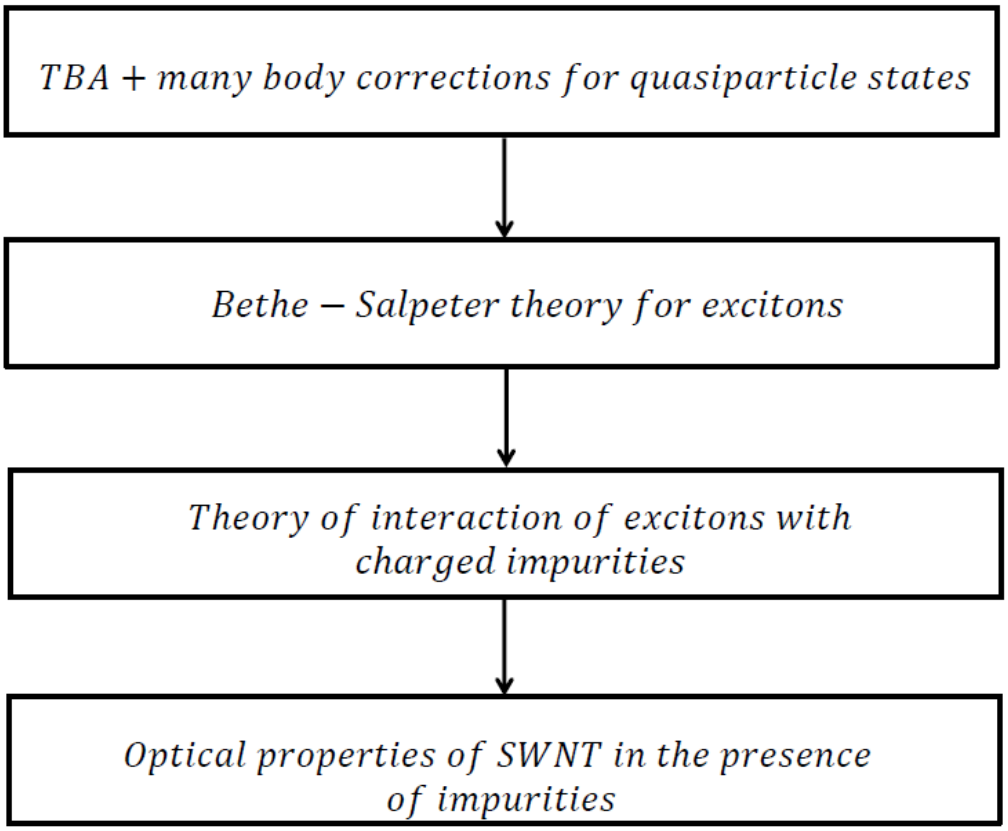

Figure 1.1: Flowchart outlining the various stages involved in computing the electronic and optical properties of SWNTs in the presence of charged impurities.

Table 1.1: Structural parameters, notations and useful quantities

Symbol	Definition	Units
a_{C-C}	C-C bond length	nm
a	lattice constant	nm
$\mathbf{a}_1, \mathbf{a}_2$	basis vectors	nm
$\mathbf{b}_1, \mathbf{b}_2$	reciprocal lattice vectors	nm^{-1}
$\mathbf{C}_h$	chiral vector	nm
d_t	tube diameter	nm
θ	chiral angle	
$\mathbf{T}$	translational vector	nm
N	number of sites in SWNT lattice	
N_c	number of unit cells in axial direction	
B	number of C atoms in supercell	
L	length of SWNT	nm
(n, m)	indices of a nanotube	
γ_{ij}	real space tight-binding matrix	eV
$a_i^\dagger$	electron creation operator	
γ	nearest neighbor hoping matrix	
$H_{TB}(k)$	tight-binding matrix in k space	eV
$H_{TB}(\mu, k)$	rotated tight-binding matrix	eV
B	number of C atoms in supercell	
μ	azimuthal quantum number	
k	axial momentum	nm^{-1}
λ	band index	
$\varepsilon_{\lambda\mu k}$	single-particle dispersion	eV
$\psi_{\lambda\mu k}$	single-particle wave function	eV
$\psi_{s\mu k}$	Bloch function	eV

Table 1.2: Structural parameters, notations and useful quantities

Symbol	Definition	Units
$C^{\lambda}_{\mu k}(s)$	tight-binding wave function coefficients	
$E_{\lambda\mu k}$	quasiparticle dispersion	eV
$\Sigma_{\lambda\mu k}$	self energy	eV
v	real space unscreened Coulomb potential	eV
w	real space screened Coulomb potential	eV
V	unscreened Coulomb matrix element	eV
W	screened Coulomb matrix element	eV
κ	environmental dielectric constant	
$\epsilon(\mathbf{r}, \mathbf{r}')$	dielectric function	
ϵ	effective dielectric constant	
E_g^0	bare band gap	eV
E_g	renormalized band gap	eV
U	on site energy	eV
S	strength of Coulomb potential	
e	electron charge	C
$(B^{(n)})^{\dagger}$	exciton creation operator	
Q	total momentum of exciton	nm^{-1}
K^d	direct Coulomb matrix	eV
K^x	exchange Coulomb matrix	eV
K^{d_1}	intra valley direct Coulomb matrix	eV
K^{d_2}	inter valley direct Coulomb matrix	eV
$\Omega^{(n)}_{\alpha}(Q)$	exciton dispersion	
$A^{(n)}_{\alpha,Q}(k)$	exciton wave function amplitude	
$\Phi^{(n)}_{\alpha,Q}(\mathbf{r}_e, \mathbf{r}_h)$	exciton wave function in real space	
$\phi_n(z)$	exciton envelop wave function	

Table 1.3: Structural parameters, notations and useful quantities

Symbol	Definition	Units
a_B	exciton Bohr radius	nm
$\mathcal{E}$	electric field vector	V m^{-1}
Z	effective charge of impurity ion	
d	distance of impurity ion above SWNT surface	nm
H_{BS}	Bethe-Salpeter Hamiltonian	eV
H_{int}	exciton-impurity interaction operator	eV
$\Psi^{(i)}(\mathbf{r}_e, \mathbf{r}_h)$	exciton scattered state	
$\mathcal{C}^{(i)}_{\alpha n Q}$	impurity wave function amplitude	
$E^{(i)}$	impurity excitation energy	eV
$S^{nm}_{\alpha,\alpha'}(Q, Q')$	scattering matrix element	eV
I_E	impurity binding energy	meV
$\vec{p}$	electron dipole operator	C m
$\vec{\eta}$	electric field polarization vector	
Γ	spectral broadening	meV
$\alpha^{ib}(\omega)$	interband absorption coefficient	cm^2
$\alpha^0(\omega)$	exciton absorption coefficient	cm^2
$\alpha(\omega)$	impurity absorption coefficient	cm^2
$\rho(\omega)$	density of states	
$\Delta\alpha(\omega)$	differential absorption coefficient	cm^2
$\delta(x)$	delta function	
$\alpha(z, \omega)$	partial absorption coefficient	cm^2
ω	photon energy	eV
c	speed of light	m s^{-1}
$\hbar$	reduced Planck constant	eV s
n_b	background refractive index	

Table 1.4: Structural parameters, notations and useful quantities

Symbol	Definition
$P(\omega)$	electric polarization
$\chi(\omega)$	optical susceptibility
$I(z)$	electric field intensity
M_{nQ}	dipole matrix element in exciton picture
$M^{(i)}$	dipole matrix element in impurity picture

Chapter 2

Survey of carbon nanotubes and their electronic properties

In this chapter, we review the basic properties of carbon nanotubes. It begins with a discussion of carbon nanotube structure and basic concepts, followed by electronic properties, including tight binding approximation and Coulomb (many-body) contribution which leads to band gap renormalization.

2.1 Carbon nanotube structure

SWNTs are tiny hollow cylinders of rolled up graphene sheets. These tubes have quite small and uniform diameter, of the order of 1 nm $=10^{-9}$ m. Because of the small diameter of a carbon nanotube ($\sim$ 1 nm) and the large length-to-diameter ratio ($> 10^4$), carbon nanotubes are an important system for studying one-dimensional physics, both theoretically and experimentally. Thus in discussing the properties of carbon nanotubes, it is assumed that the carbon nanotube is a one-dimensional crystal with a translation vector $\mathbf{T}$ along the cylinder axis and a number of carbon hexagons associated with the circumferential direction, indexed by the chiral vector ($\mathbf{C}_h$), as is shown on Fig. 2.1.

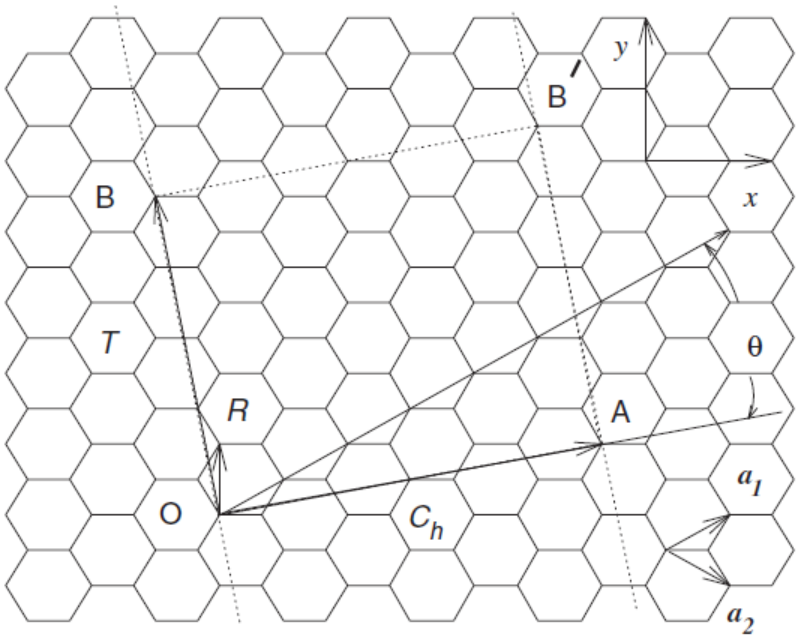

Figure 2.1: An unrolled nanotube unit cell projected on the graphene layer. When the nanotube is rolled up, the chiral vector $\mathbf{C}_h$ turns into the circumference of the cylinder, and the translation vector $\mathbf{T}$ is aligned along the axis of the cylinder, and θ is the chiral angle. The unit vectors $(\mathbf{a}_1, \mathbf{a}_2)$ of the graphene layer are indicated in the figure along with the inequivalent A and B sites within the unit cell of the graphene layer given by a hexagon. In the present example, a (4,2) nanotube is under construction. The unit cell of the nanaotube is defined by the rectangle delimited by the vectors $\mathbf{C}_h$ and $\mathbf{T}$.

2.1.1 Nanotube geometry and the chiral indices

A single wall carbon nanotube (SWNT) is constructed starting from a strip of a graphene layer (see Fig. 2.1) by rolling it up into a seamless cylinder [1]. The nanotube structure is uniquely determined by the chiral vector C_h which spans the circumference of the cylinder when the graphene layer is rolled up into a tube. The chiral vector can be written in the form $\mathrm{C}_h = n\mathbf{a}_1 + m\mathbf{a}_2$, where the vectors $\mathbf{a}_1$ and $\mathbf{a}_2$ are unit vectors of the hexagonal honeycomb lattice (see Fig. 2.1) which contains the two distinct carbon atom sites A and B. The values of n and m are

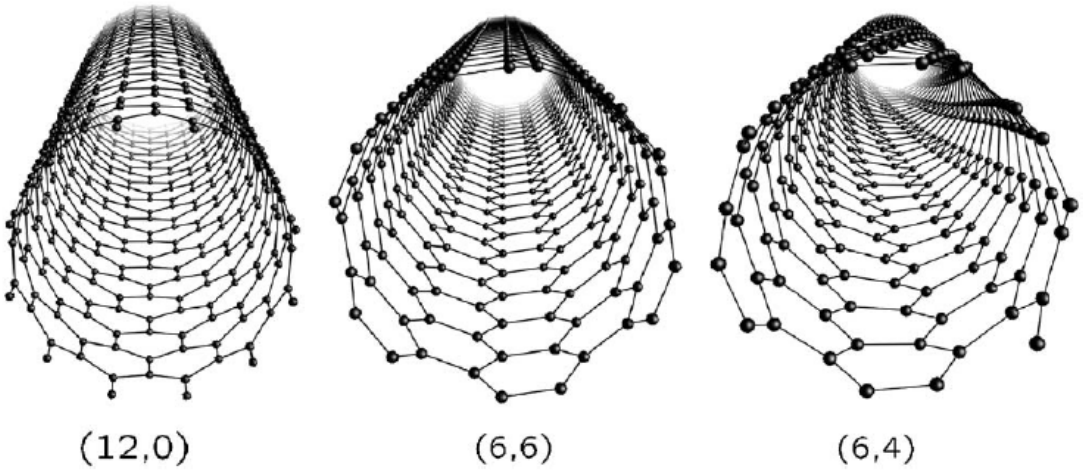

Figure 2.2: Atomic structures of (12,0) zigzag tubes, (6,6) armchair, and (6,4) chiral nanotubes.

arbitrary integer numbers which uniquely characterize the nanotube structure. In the shortened (n, m) form, the chiral vector is written as a pair of integers and the same notation is widely used to characterize the geometry of each distinct (n, m) nanotube [1].

This chiral vector C_h defines the circumference of the tube. The diameter d_t of the nanotube can thus be estimated from

$$d_t = \frac{|\mathbf{C}_h|}{\pi} = \frac{a}{\pi}\sqrt{n^2 + nm + m^2} \tag{2.1}$$

where $a = \sqrt{3}a_{C-C} \simeq 0.249$ nm is the lattice constant for the graphene layer and $a_{C-C} = 0.144$ nm is the nearest neighbor C-C distance. The chiral vector C_h uniquely defines a particular tube (n, m) tube, as well as its chiral angle θ, which is the angle between C_h and $\mathbf{a}_1$ (zigzag direction of the graphene sheet, see Fig. 2.1). As one can derive from Fig. 2.1, the chiral angle θ can be expressed as

$$\cos\theta = \frac{\mathrm{C}_h \cdot \mathbf{a}_1}{|\mathrm{C}_h||\mathbf{a}_1|} = \frac{2n + m}{2\sqrt{n^2 + nm + m^2}} \tag{2.2}$$

As an example, the chiral vector C_h shown in Fig. 2.1 is given by $\mathrm{C}_h = 4\mathbf{a}_1 + 2\mathbf{a}_2$, and thus the corresponding nanotube can be identified by the pair of integers (n, m)

= (4, 2). In general, the nanotube physical properties depend on how the graphene sheet is rolled up, and from a symmetry point of view, two types of nanotubes can be formed, namely the achiral armchair or zigzag tubes, and the chiral tubes. Using the (n, m) scheme, the nanotubes are classified as chiral ($0 < m < n$) and achiral ($m = 0$ or $m = n$), which in turn are known as zigzag ($m = 0$) and armchair ($m = n$) nanotubes (Fig. 2.2).

2.1.2 Lattice vectors in real space

The geometry of the graphene lattice and the chiral vector determine not only the diameter of the tube, but also the unit cell and its number of carbon atoms. The smallest graphene lattice vector $\mathbf{T}$ perpendicular to $\mathbf{C}_h$ defines the translational period T along the tube axis. The lattice vector $\mathbf{T}$ can also be expressed in terms of the basis vectors $\mathbf{a}_1$ and $\mathbf{a}_2$ as $\mathrm{T} = t_1\mathbf{a}_1 + t_2\mathbf{a}_2$. Using $\mathbf{C}_h \cdot \mathbf{T} = 0$, the expressions for t_1 and t_2 are given by

$$t_1 = \frac{2n + m}{N_R}, \quad t_2 = -\frac{2m + n}{N_R} \tag{2.3}$$

where N_R is the greatest common divisor (gcd) of $(2n + m)$ and $(2m + n)$. The length of the translational vector T is given by

$$T = |\mathbf{T}| = \frac{\sqrt{3}a}{N_R}\sqrt{n^2 + nm + m^2} \tag{2.4}$$

For armchair and zigzag achiral tubes, $T = a$ and $\sqrt{3}a$ respectively. The unit cell of an unrolled nanotube on a graphene layer is a rectangle bounded by the vectors $\mathbf{C}_h$ and $\mathbf{T}$ (see the rectangle shown in Fig. 2.1 for the (4,2) nanotube). The area of the nanotube unit cell can be easily calculated as a vector product of these two vectors, $|\mathbf{C}_h \times \mathbf{T}| = \sqrt{3}a^2(n^2 + nm + m^2)/N_R$. Dividing this product by the area of the unit cell of a graphene layer $|\mathbf{a}_1 \times \mathbf{a}_2| = \sqrt{3}a^2/2$, one gets the number of hexagons in the unit cell of a nanotube,

$$N = \frac{2(n^2 + nm + m^2)}{N_R} \tag{2.5}$$

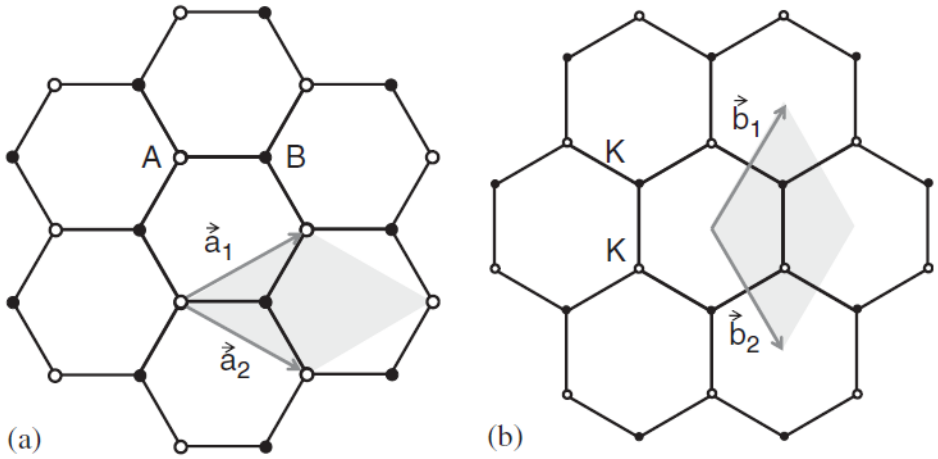

Figure 2.3: (a) Real space lattice of a graphene layer. The rhombus represents the graphene unit cell with lattice vectors $\mathbf{a}_1$ and $\mathbf{a}_2$ delimiting it. Note that this area encloses a total of 2 atoms, one A atom and one B atom. (b) Reciprocal space lattice of the a graphene layer showing the unit vectors $\mathbf{b}_1$ and $\mathbf{b}_2$. Note also that the reciprocal space structure has two inequivalent points K and K'.

Accordingly, the number of carbon atoms in the unit carbon atoms per unit cell N_c is given by

$$N_c = 2N = \frac{4(n^2 + nm + m^2)}{N_R} \tag{2.6}$$

For a (4,2) nanotube we have $N = 28$, so that the unit cell of the $(4, 2)$ nanotube (see the rectangle shown in Fig. 2) contains 28 hexagons, or $2 \times 28 = 56$ carbon atoms. For armchair (n, m) and zigzag $(n, 0)$ tubes, $N = 2n$.

2.1.3 Lattice vectors in reciprocal space

The graphene reciprocal lattice unit vectors $\mathbf{b}_1$ and $\mathbf{b}_2$ can be constructed from the real space vectors $\mathbf{a}_1$ and $\mathbf{a}_2$ using the standard definition $\mathbf{a}_i \cdot \mathbf{b}_j = 2\pi\delta_{ij}$, where δ_{ij} is the Kroneker delta symbol. In Figs. 2.3(a) and (b) we show the real and reciprocal space lattice of a graphene sheet, correspondingly. Note the $30\,^\circ$ difference in orientation of the hexagons in real space with respect to those of the reciprocal

Symbol	Name	Formula
a	lattice constant	$a = \sqrt{3}a_{C-C} \simeq 0.249$ nm
$\mathbf{a}_1, \mathbf{a}_2$	basis vectors	$\left(\frac{\sqrt{3}}{2}, \frac{1}{2}\right)a, \quad \left(\frac{\sqrt{3}}{2}, -\frac{1}{2}\right)a$
$\mathbf{b}_1, \mathbf{b}_2$	reciprocal lattice vectors	$\left(\frac{1}{\sqrt{3}}, 1\right)\frac{2\pi}{a}, \quad \left(\frac{1}{\sqrt{3}}, -1\right)\frac{2\pi}{a}$
$\mathbf{C}_h$	chiral vector	$\mathrm{C}_h = m\mathbf{a}_1 + n\mathbf{a}_2 = (n, m)$
d_t	tube diameter	$d_t = \frac{\lvert\mathbf{C}_h\rvert}{\pi} = \frac{a}{\pi}\sqrt{n^2 + nm + m^2}$
θ	chiral angle	$\cos\theta = \frac{2n+m}{2\sqrt{n^2+nm+m^2}}$
$\mathbf{T}$	translational vector	$\mathrm{T} = t_1\mathbf{a}_1 + t_2\mathbf{a}_2 = (t_1, t_2)$
N_C	number of C atoms per unit cell	$N_c = \frac{4(n^2+nm+m^2)}{N_R}$

Table 2.1: Structural parameters for an (n, m) SWNT. Here, n, m, t_1 ,t_2 are integers and $N_R = \gcd(2n + m, 2m + n)$, where $\gcd(n, m)$ denotes the greatest common divisor of (n, m).

space. In Table 2.1, we summarize the main structure parameters of an (n, m) SWNT.

2.2 Electronic structure of SWNTs in tight binding approximation (TBA)

The TBA model Hamiltonian [1, 63] is given by

$$H_0 \;=\; \sum_{ij} \gamma_{ij} a_i^\dagger a_j \tag{2.7}$$

where the summation on i, j runs over the total number of sites in the SWNT. The total number of sites is given by $N = N_c B$, where N_c is the total number of unit cells in the SWNT crytal and B the number of carbon atoms in each unit cell, a_i is an electron annihilation operator at the atomic site i, $\gamma_{ij} = \gamma \simeq 2.9$ eV is the hopping

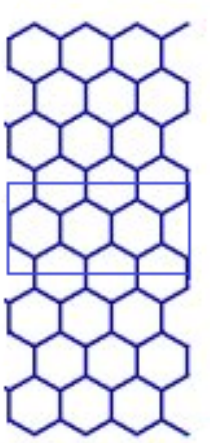

Figure 2.4: Unscrolled unit cell of a (3,0) SWNT

integral with the sum taken over nearest-neighbor carbon atoms in the SWNT, and γ is approximately equal for all neighbors. Because of translation symmetry, the Hamiltonian H_0 which originally is an $N \times N$ matrix can be reduced to form

$$H_{TB}(k) = \sum_{s,s'} \gamma_{s,s'}(k) a^{\dagger}_{sk} a_{s'k} \tag{2.8}$$

where the summation on s, s' now runs over the number of atoms in the unit cell B. The Hamiltonian H_{TB} includes connectivity information for the carbon atoms of the unit cell and has dimension $B \times B$. For realistic SWNTs, the matrix of H_{TB} is very large. The (3,0) SWNT is perhaps unrealistically narrow, but it has a small enough unit cell to readily demonstrate the form of H_{TB}. In Fig. 2.4, we show the unscrolled unit cell of a (3,0) nanotube. It has 12 atoms in the unit cell and thus

Hamiltonian H_{TB} for this tube is a 12×12 matrix:

$$H_{TB}(k) = \gamma \begin{pmatrix} 0 & 0 & 0 & 1 & 1 & 0 & 0 & 0 & 0 & e^{-ikT} & 0 & 0 \\ 0 & 0 & 0 & 0 & 1 & 1 & 0 & 0 & 0 & 0 & e^{-ikT} & 0 \\ 0 & 0 & 0 & 1 & 0 & 1 & 0 & 0 & 0 & 0 & 0 & e^{-ikT} \\ 1 & 0 & 1 & 0 & 0 & 0 & 1 & 0 & 0 & 0 & 0 & 0 \\ 1 & 1 & 0 & 0 & 0 & 0 & 0 & 1 & 0 & 0 & 0 & 0 \\ 0 & 1 & 1 & 0 & 0 & 0 & 0 & 0 & 1 & 0 & 0 & 0 \\ 0 & 0 & 0 & 1 & 0 & 0 & 0 & 0 & 0 & 1 & 0 & 1 \\ 0 & 0 & 0 & 0 & 1 & 0 & 0 & 0 & 0 & 1 & 1 & 0 \\ 0 & 0 & 0 & 0 & 0 & 1 & 0 & 0 & 0 & 0 & 1 & 1 \\ e^{ikT} & 0 & 0 & 0 & 0 & 0 & 1 & 1 & 0 & 0 & 0 & 0 \\ 0 & e^{ikT} & 0 & 0 & 0 & 0 & 0 & 1 & 1 & 0 & 0 & 0 \\ 0 & 0 & e^{ikT} & 0 & 0 & 0 & 1 & 0 & 1 & 0 & 0 & 0 \end{pmatrix} \tag{2.9}$$

where T is the translational period and k the axial component of the wave vector as discussed below. To obtain properly symmeterized analytic wave functions, it is possible to reduce the large $B \times B$ TB Hamiltonian to a 4×4 problem by choosing a unit cell with four carbon atoms and exploiting the rotational symmetry of the SWNT. Under this operation, the reduced Hamiltonian for a zig zag (n,0) tube becomes

$$H_{TB}(\mu, k) = \gamma \begin{pmatrix} 0 & 2\cos(\frac{\pi\mu}{n}) & 0 & e^{-ikT} \\ 2\cos(\frac{\pi\mu}{n}) & 0 & 1 & 0 \\ 0 & 1 & 0 & 2\cos(\frac{\pi\mu}{n}) \\ e^{ikT} & 0 & 2\cos(\frac{\pi\mu}{n}) & 0 \end{pmatrix} \tag{2.10}$$

where μ the azimuthal quantum number which takes integer values in the interval $(-n/2, n/2]$. The eigenvectors of $H_{TB}(\mu, k)$ are given by

$$\mathbf{C}^{\lambda}_{\mu k} = \frac{1}{\sqrt{2}} \begin{bmatrix} \frac{1}{\sqrt{2}} \begin{pmatrix} \frac{\Gamma_{\mu k}}{|\Gamma_{\mu k}|} \\ \lambda \end{pmatrix} \\ \frac{1}{\sqrt{2}}\, e^{ikT/2} \begin{pmatrix} \frac{\Gamma_{\mu k}}{|\Gamma_{\mu k}|} \\ \lambda \end{pmatrix} \end{bmatrix} \tag{2.11}$$

where $\lambda = \pm$ represents the conduction and valence bands and

$$\Gamma_{\mu k} = 2\cos\left(\frac{\pi\mu}{n}\right) - e^{-ikT/2} \tag{2.12}$$

The eigenvalues are

$$\begin{aligned} \varepsilon_{\lambda\mu k} &= \lambda\gamma|\Gamma_{\mu k}| \\ &= \lambda\gamma\sqrt{1 + 4\cos^2\left(\frac{\pi\mu}{n}\right) - 4\cos\left(\frac{\pi\mu}{n}\right)\cos\left(\frac{kT}{2}\right)} \end{aligned} \tag{2.13}$$

The corresponding single particle states $\psi_{\lambda\mu k}(\mathbf{r})$ can be written in TBA in the form [1]

$$\psi_{\lambda\mu k}(\mathbf{r}) = \sum_{s=1}^{4} C^{\lambda}_{\mu k}(s)\psi_{s\mu k}(\mathbf{r}), \quad \lambda = c, v \tag{2.14}$$

as linear combinations of the Bloch functions $\psi_{sk}(\mathbf{r})$. Using four atoms per unit cell in the SWNT we derive:

$$\begin{aligned} \psi_{s\mu k}(\mathbf{r}) &= \frac{1}{\sqrt{4n}}\frac{1}{\sqrt{N_c}} \sum_{j=-N_c/2}^{N_c/2} \sum_{i'=-n/2}^{n/2} e^{ik(z_s+Tj)} \times \\ &\quad \times e^{i\mu(\theta_s+2\pi i'/n)} U(\mathbf{r} - \mathbf{R}_{si'j}), \quad s = 1, \ldots, 4 \end{aligned} \tag{2.15}$$

where N_c is the number of unit cells in the finite length $(n, 0)$ zigzag SWNT defined as the ratio of the length of the SWNT and the unit cell length, T (i.e., $L = N_c T$). The coefficients $C^{\lambda}_{\mu k}(s)$ are the TBA wave function amplitudes, the function $U(\mathbf{r} - \mathbf{R}_{si'j})$ represents the atomic orbital localized on site $si'j$, k is the axial momentum, defined such that

$$-\frac{\pi}{T} \leq k < \frac{\pi}{T} \tag{2.16}$$

The electronic states of SWNTs can thus be labeled by the quantum numbers (μ, k). In general, μ is not conserved. For ziz zag (n,0) tubes for instance, μ changes to

$$\mu \rightarrow \text{Mod}\ [2n, n + \mu]$$

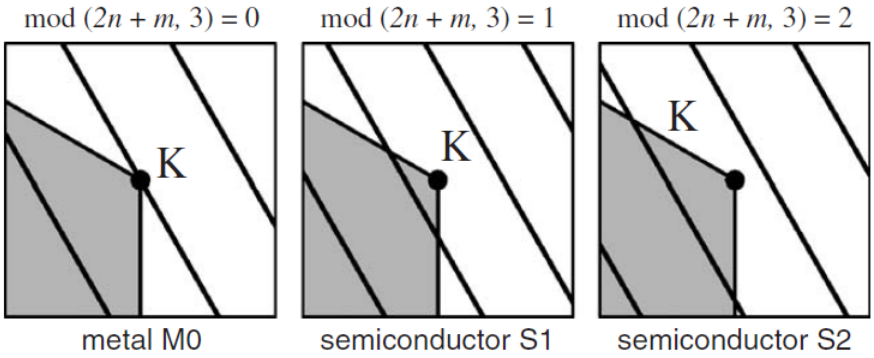

Figure 2.5: Three different configurations of the cutting lines in the vicinity of the K point. The first configuration $\mathrm{mod}(2n+m,3)=0$ corresponds to the case of metallic nanotubes M0, and the last two configurations, $\mathrm{mod}(2n+m,3)=1$ and $\mathrm{mod}(2n+m,3)=2$, correspond to the case of semiconducting nanotubes of types S1 and S2, respectively [13].

once we cross the boundaries of the Brillouin zone (BZ), i.e. the interval

$$-\frac{\pi}{T} < k \leq \frac{\pi}{T}$$

Such a process is called an Umklapp process [2] and must be well accounted for once the BZ boundary is crossed.

Depending on the tube symmetry, that is, on the chiral vector $\mathbf{C}_h = (n, m)$, we can have either metallic or semiconducting nanotubes. This can be further explained using the concept of cutting lines [13]. The cutting line approach has been successfully used to predict the metallic or semiconducting nature of the nanotubes. In this approach, the nanotube energy bands are determined from those of graphene by means of the zone folding scheme [1]. Since the graphene valence and conduction bands cross at the K and K' points in the Brillouin zone, carbon nanotubes for which one of the cutting lines crosses the K or K' points should have a metallic behavior. In contrast, carbon nanotubes for which none of the cutting line passes through the K or K' points, show a band gap, and thus show semiconducting behavior. The cutting lines in the vicinity of the K are shown in Fig. 2.5 for three different cases, $\mathrm{mod}(2n+m,3)=0$, $\mathrm{mod}(2n+m,3)=1$, and $\mathrm{mod}(2n+m,3)=2$. The first case, $\mathrm{mod}(2n+m,3)=0$, corresponds to the cutting line crossing

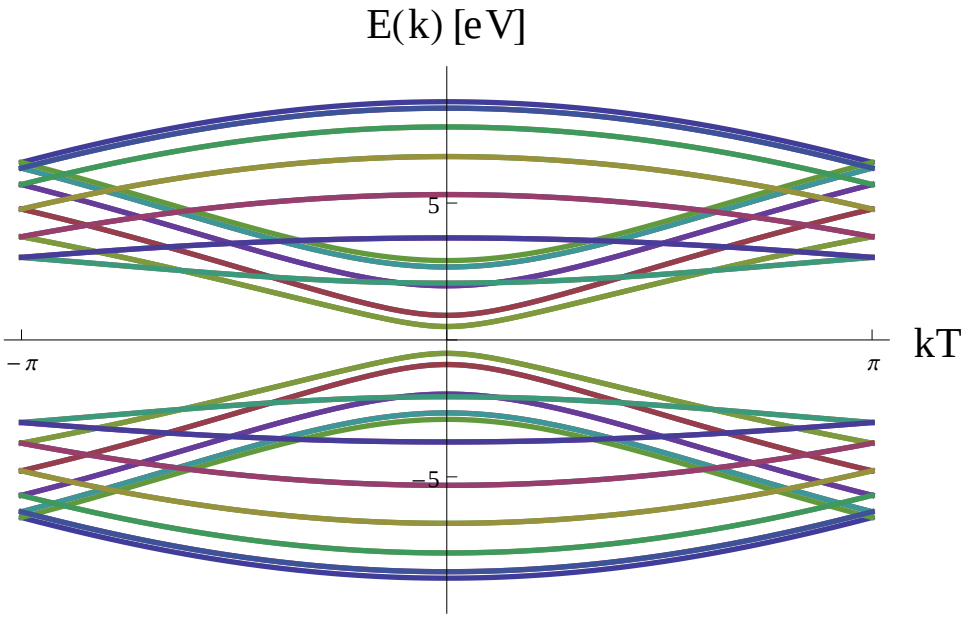

Figure 2.6: Electronic band structure of an (11,0) SWNT calculated using the nearest neighbor tight-binding approximation [1].

the K point, resulting in metallic behavior, as discussed above. The other two configurations $\mathrm{mod}(2n+m,3)=1$, and $\mathrm{mod}(2n+m,3)=2$, correspond to the case of semiconducting tubes.

The simple electronic band structure consideration discussed so far does not give the correct band gap. A constant energy difference was found between the experimental and calculated results, which could be attributed to many-body corrections (as discussed below) which are not taken into account in the tight binding approximation [12, 15]. In Fig. 2.6, we show the electronic band structure of an (11,0) SWNT computed in the nearest-neighbor TB approximation. In the next chapter, we will discuss the importance of many-body effects in the electronic and optical properties of SWNTs.

Chapter 3

Many-body effects in single-walled nanotubes

Enhanced Coulomb interaction in one-dimensional systems like carbon nanotubes has been shown to be an essential ingredient for the modeling of the electronic and optical properties of these materials [15,16]. Coulomb effects affect these properties in two main ways: through the band gap renormalization due to electron-electron interaction and by the formation of bound excitons due to electron-hole coupling. In this chapter, we discuss the renormalization of the electronic structure of SWNTs and the theory of excitons.

3.1 Band gap renormalization in carbon nanotubes

Strong electron-electron interaction in SWNTs leads to band gap renormalization. The many-body contribution to the band structure is incorporated by including the electron and hole self-energies within the screened Hartree Fock theory [64,65]. The electron quasi particle energy is given by including the self-energy contributions (see Fig. 3.1):

$$E_{c\mu k} = \varepsilon_{c\mu k} + \Sigma_{c\mu k} \tag{3.1}$$

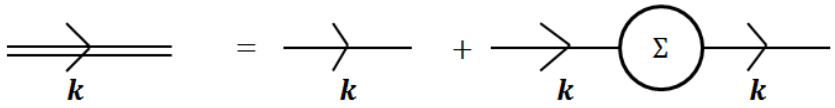

Figure 3.1: Propagator of an electron in an interacting system: double line is the quasi particle energy, single line is the free propagator, and Σ is reducible self energy. Σ is the sum of different irreducible energies. In the Hartree-Fock approximation, we keep only the lowest order self-energy terms which are the direct (Hartree) and exchange (Fock) self-energies.

with $\varepsilon_{c\mu k}$ the single-particle energy and $\Sigma_{c\mu k}$ the electron self-energy

$$\Sigma_{c\mu k} = \sum_{\mathbf{l}} \left\{ W(\overset{c\,v\,v\,c}{\mathbf{kl}|\mathbf{lk}}) - W(\overset{v\,c\,v\,c}{\mathbf{lk}|\mathbf{lk}}) \right\} \tag{3.2}$$

where $\mathbf{k} = (\mu, k)$ is the wave vector and W the static screened Coulomb interaction as discussed below. In an analogous manner, the hole quasiparticle energy is given by

$$E_{v\mu k} = \varepsilon_{v\mu k} + \Sigma_{v\mu k} \tag{3.3}$$

where the hole self energy is expressed as

$$\Sigma_{v\mu k} = \sum_{\mathbf{l}} \left\{ W(\overset{v\,v\,v\,v}{\mathbf{kl}|\mathbf{lk}}) - W(\overset{v\,v\,v\,v}{\mathbf{lk}|\mathbf{lk}}) \right\} \tag{3.4}$$

The general expression for the Coulomb matrix element W is

$$W(\overset{\lambda_1\,\lambda_2\,\lambda_3\,\lambda_4}{\mathbf{k_1}\mathbf{k_2}|\mathbf{k_3}\mathbf{k_4}}) = \int \psi^*_{\lambda_1\mathbf{k}_1}(\mathbf{r})\psi^*_{\lambda_2\mathbf{k}_2}(\mathbf{r}')w(\mathbf{r}-\mathbf{r}')\psi_{\lambda_3\mathbf{k}_3}(\mathbf{r}')\psi_{\lambda_4\mathbf{k}_4}(\mathbf{r})\,d\mathbf{r}d\mathbf{r}' \tag{3.5}$$

The screened Coulomb potential is given by

$$w(\mathbf{r},\mathbf{r}') = \frac{v(\mathbf{r},\mathbf{r}')}{\kappa\epsilon(\mathbf{r},\mathbf{r}')} \tag{3.6}$$

where κ is the environmental dielectric constant, and $\epsilon(\mathbf{r},\mathbf{r}')$ is the dielectric function that describes the screening from the core electrons. v is the bare Coulomb

interaction and is given by

$$v(\mathbf{r},\mathbf{r}') = \frac{e^2}{|\mathbf{r}-\mathbf{r}'|} \tag{3.7}$$

The Coulomb matrix element $W(\overset{\lambda_1}{\mathbf{k_1}}\overset{\lambda_2}{\mathbf{k_2}}|\overset{\lambda_3}{\mathbf{k_3}}\overset{\lambda_4}{\mathbf{k_4}})$ is expressed as

$$W(\overset{\lambda_1}{\mathbf{k_1}}\overset{\lambda_2}{\mathbf{k_2}}|\overset{\lambda_3}{\mathbf{k_3}}\overset{\lambda_4}{\mathbf{k_4}}) = \frac{V(\overset{\lambda_1}{\mathbf{k_1}}\overset{\lambda_2}{\mathbf{k_2}}|\overset{\lambda_3}{\mathbf{k_3}}\overset{\lambda_4}{\mathbf{k_4}})}{\kappa\varepsilon(\mathbf{k}_4-\mathbf{k}_1)} \tag{3.8}$$

where $\epsilon(\mathbf{k}_4-\mathbf{k}_1)$ is the Fourier transform of $\epsilon(\mathbf{r},\mathbf{r}')$, and $V(\overset{\lambda_1}{\mathbf{k_1}}\overset{\lambda_2}{\mathbf{k_2}}|\overset{\lambda_3}{\mathbf{k_3}}\overset{\lambda_4}{\mathbf{k_4}})$ the unscreened Coulomb interaction which can be defined by replacing w in Eq. (3.5) by v. The Coulomb matrix elements $V(\overset{\lambda_1}{\mathbf{k_1}}\overset{\lambda_2}{\mathbf{k_2}}|\overset{\lambda_3}{\mathbf{k_3}}\overset{\lambda_4}{\mathbf{k_4}})$ are calculated within the TBA. Applying the TBA single-particle wave functions (Eq. 2.14) yields

$$V(\overset{\lambda_1}{\mathbf{k_1}}\overset{\lambda_2}{\mathbf{k_2}}|\overset{\lambda_3}{\mathbf{k_3}}\overset{\lambda_4}{\mathbf{k_4}}) = \sum_{s,s'} C^{\lambda_1 *}_{\mathbf{k}_1}(s) C^{\lambda_2 *}_{\mathbf{k}_2}(s') C^{\lambda_3}_{\mathbf{k}_3}(s') C^{\lambda_4}_{\mathbf{k}_4}(s) v_{s,s'}(\Delta\mu,\Delta q)\delta_{\mathbf{k}_4-\mathbf{k}_1,\mathbf{k}_2-\mathbf{k}_3} \tag{3.9}$$

where the coefficients $C^{\lambda}_{\mathbf{k}}(s)$ are the TB coefficients. The conservation of the momentum is expressed by the Kronecker delta δ. The Fourier transform of the Coulomb potential is given by

$$\begin{aligned} v_{s,s'}(\Delta\mu,\Delta q) &= \frac{1}{4nN_c}\sum_{i'=-n/2}^{n/2}\sum_{j=-N_c/2}^{N_c/2} e^{i\Delta\mu(\theta_s-\theta_{s'}+\frac{2\pi i'}{n})} e^{i\Delta q(z_s-z_{s'}+jT)} \times \\ &\qquad \times v_{s,s'}(i',j) \end{aligned} \tag{3.10}$$

with the momentum transfer $(\Delta\mu,\Delta q) = (\mu_4-\mu_1, k_4-k_1)$, and

$$\begin{aligned} v_{s,s'}(i',j) &= v(|\mathbf{R}_{si'j}-\mathbf{R}_{s'00}|) \\ &= \frac{e^2}{\sqrt{4R^2\sin^2(\theta_s-\theta_{s'}+\frac{2\pi i'}{n})+(z_s-z_{s'}+jT)^2}} \end{aligned} \tag{3.11}$$

where $\mathbf{R}_{si'j}$ is the lattice vector, $j = j_e - j_h$ is the relative axial coordinate, and $i' = i_e - i_h$ the relative circumferential coordinate.

An ideal calculation for the band gap renormalization and the excitation spectra of excitons in SWNTs in general would include an appropriate treatment of the

(n,m)	$d_t(nm)$	family	E_g^0 (eV)	$S = 2.12$	$S = 1.15$	$S = 0.42$	$S = 0.04$
(4,0)	0.32	2	2.40	5.04	3.84	2.93	2.45
(5,0)	0.40	1	2.22	3.97	3.17	2.57	2.25
(7,0)	0.55	2	1.43	3.41	2.51	1.83	1.47
(8,0)	0.63	1	1.36	2.54	2.00	1.60	1.38
(10,0)	0.79	2	1.02	2.64	1.90	1.34	1.05
(11,0)	0.87	1	0.98	1.84	1.45	1.15	1.00
(13,0)	1.03	2	0.79	2.19	1.55	1.07	0.82
(14,0)	1.11	1	0.77	1.43	1.13	0.90	0.78
(16,0)	1.27	2	0.64	1.90	1.33	0.89	0.67
(17,0)	1.35	1	0.63	1.15	0.91	0.73	0.64
(19,0)	1.51	2	0.54	1.68	1.17	0.77	0.57
(20,0)	1.59	1	0.53	0.95	0.76	0.62	0.54
(25,0)	1.98	1	0.42	1.40	0.95	0.61	0.43

Table 3.1: Renormalized band gap (in eV) for different families $r = \mathrm{Mod}(2\mathrm{n} + \mathrm{m}, 3)$ of (n,0) tubes, calculated for different Coulomb potential strengths ($S = U/\epsilon\gamma$). The fourth column gives the bare band gap calculated using a π-orbital only tight-binding model.

dielectric function $\epsilon(\mathbf{r}, \mathbf{r}')$ [17, 66]. For computational purposes, we replace this complicated response function with a single static dielectric constant ϵ:

$$\epsilon \approx \kappa\epsilon(\mathbf{r}, \mathbf{r}') \tag{3.12}$$

describing the environmental screening and partially including the SWNT screening. This approximation has been shown to be most accurate for narrow tubes, and for embedding media with large dielectric constant. In this regime, the exciton length along the tube is large relative to the tube radius, and most of the dielectric screening occurs in the surrounding medium [67, 68]. The screening is then well described by the dielectric constant ϵ of the nanotube environment. For isolated nanotubes, or tubes in low-ϵ media, this treatment is not very accurate.

Coulomb interaction in one-dimensional structures needs to be treated with care due to logarithmic divergences. This problem can be avoided by introducing a regularized Coulomb potential. Accordingly, the unscreened Coulomb potential is

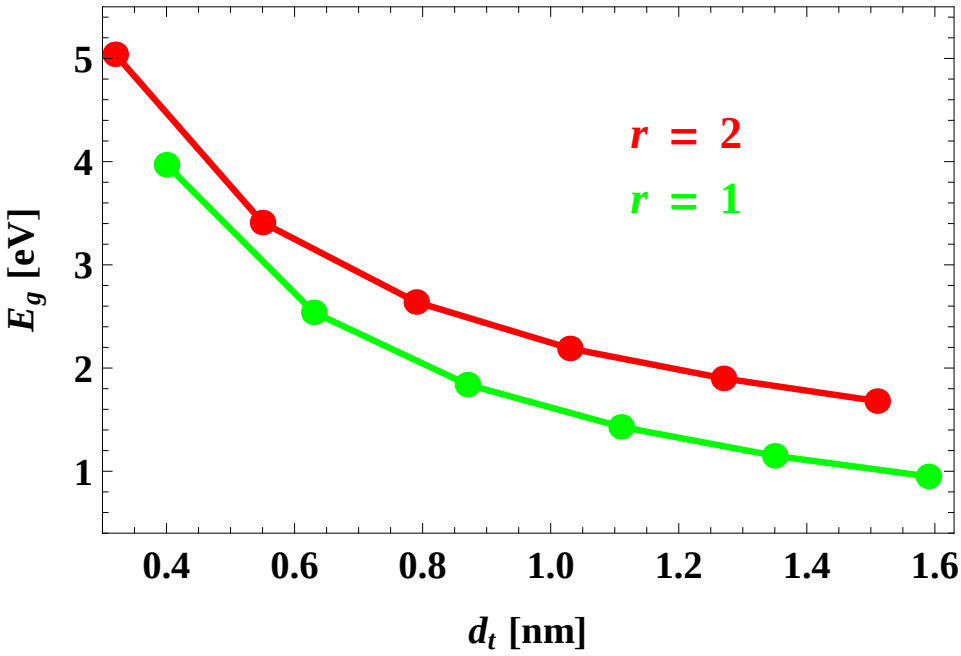

Figure 3.2: Renormalized band gap for different $(n, 0)$ SWNTs for $\epsilon = 2$. Red and green points indicate zigzag tubes of different families.

modeled by the Ohno potential [66]

$$v_{s,s'}(i', j) = \frac{U}{\sqrt{\left(\frac{U}{e^2}|\mathbf{R}_{si'j} - \mathbf{R}_{s'00}|\right)^2 + 1}} \tag{3.13}$$

where U is the on site energy (energy cost to place two electrons on a single site) and is taken to $U = 11.3$ eV for π orbitals [66]. The screened Coulomb interaction is accordingly

$$w_{s,s'}(i', j) = \frac{v_{s,s'}(i', j)}{\epsilon} \tag{3.14}$$

To illustrate the importance of Coulomb effects in SWNTs, Table 3.1 gives the renormalized band gap for zig-zag tubes placed in different dielectric media calculated by including the quasi particle self energy corrections. The effect of screening is controlled by the parameter ϵ which determines the strength of the Coulomb interaction. The strength of the Coulomb potential is defined by the dimensionless

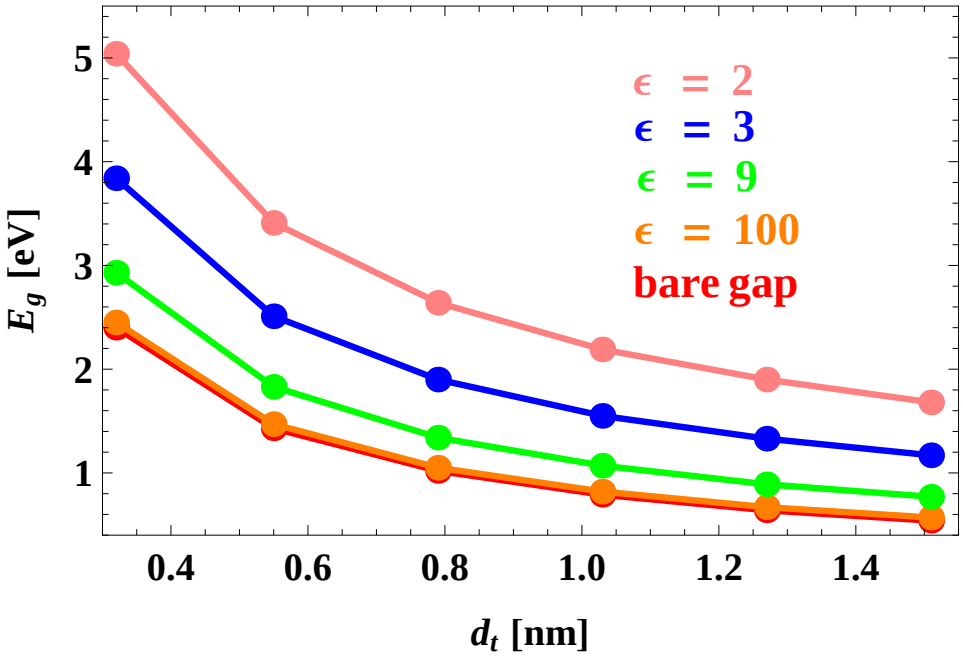

Figure 3.3: Renormalized band gap as a function of tube diameter d_t for $r = 2$ plotted for different dielectric media: (Pink) is for $\epsilon = 2$; (Blue) for $\epsilon = 3$; (Green) for $\epsilon = 9$; (Orange) for $\epsilon = 100$; and (Red) is the bare band gap. It shows that many-body effects become less important for SWNTs embedded in high dielectric media.

parameter $S = U/\epsilon\gamma$, where γ is nearest-neighbor hopping integral which defines the energy scale. In Fig. 3.2, we show the family splitting of the renormalized band gap for selected $(n, 0)$ SWNTs computed for $\epsilon = 2$. Fig. 3.3 shows the band gap for tubes embedded in different dielectric media. Because SWNTs consist of singular tubular sheets, all carbon atoms and conduction electron states reside on the surface and thus, the electronic properties of semiconducting SWNTs are highly susceptible to minute changes in the local electrostatic environment. In what follows, we review the Bethe-Salpeter theory for excitons.

3.2 Theory of excitons in SWNTs by Bethe-Salpeter Equation (BSE)

The exciton creation operator for the n^{th} excitation is [86]

$$(B^{(n)})^\dagger = \sum_{\mathbf{k}_e,\mathbf{k}_h} A_{cv}^{(n)}(\mathbf{k}_e,\mathbf{k}_h) a^\dagger_{c\mathbf{k}_e} d^\dagger_{v\mathbf{k}_h} \tag{3.15}$$

where $a^\dagger_{c\mathbf{k}_e}$ ($d^\dagger_{v\mathbf{k}_h}$) denotes the creation operator of the electron (hole), c (v) is the conduction (valence) band index, and the wave vector $\mathbf{k}_e = (\mu_e, k_e)$. The expansion coefficients $A_{cv}^{(n)}(\mathbf{k}_e,\mathbf{k}_h)$, which will have to be determined are the exciton wave function amplitudes. The wave function describing the correlated motion of the electron-hole pair can thus be expressed as

$$\begin{aligned} \Phi^{(n)}(\mathbf{r}_e,\mathbf{r}_h) &= \langle \mathbf{r}_e,\mathbf{r}_h|(B^{(n)})^\dagger|0\rangle \\ &= \sum_{\mathbf{k}_e,\mathbf{k}_h} A_{cv}^{(n)}(\mathbf{k}_e,\mathbf{k}_h)\psi_{c\mathbf{k}_e}(\mathbf{r}_e)\psi^*_{v\mathbf{k}_h(\mathbf{r}_h)} \end{aligned} \tag{3.16}$$

The total Hamiltonian of the system is given by

$$H = H(\mathbf{r}_e) + H(\mathbf{r}_h) - \frac{e^2}{|\mathbf{r}_e - \mathbf{r}_h|} \tag{3.17}$$

where

$$H(\mathbf{r}_e) = \frac{\mathbf{p}_e^2}{2m} + V_{eff}(\mathbf{r}_e) \tag{3.18}$$

Here, $V_{eff}(\mathbf{r}_e)$ is an effective one body potential that has the periodicity of the lattice so that

$$H(\mathbf{r}_e)\psi_{c\mathbf{k}_e}(\mathbf{r}_e) = E_{c\mathbf{k}_e}\psi_{c\mathbf{k}_e}(\mathbf{r}_e) \tag{3.19}$$

By applying the Hamiltonian operator (Eq. 3.17) to the wave function (Eq. 3.16), we obtain the equation of motion for the expansion coefficients $A_{cv}^{(n)}(\mathbf{k}_e,\mathbf{k}_h)$:

$$\begin{aligned} \Delta_{cv}(\mathbf{k}_e,\mathbf{k}_h)A_{cv}^{(n)}(\mathbf{k}_e,\mathbf{k}_h) + \sum_{\mathbf{k}'_e\mathbf{k}'_h} K(c\mathbf{k}_e, v\mathbf{k}_h; c\mathbf{k}'_e, v\mathbf{k}'_h)A_{cv}^{(n)}(\mathbf{k}'_e,\mathbf{k}'_h) \\ = \Omega_n A_{cv}^{(n)}(\mathbf{k}_e,\mathbf{k}_h) \end{aligned} \tag{3.20}$$

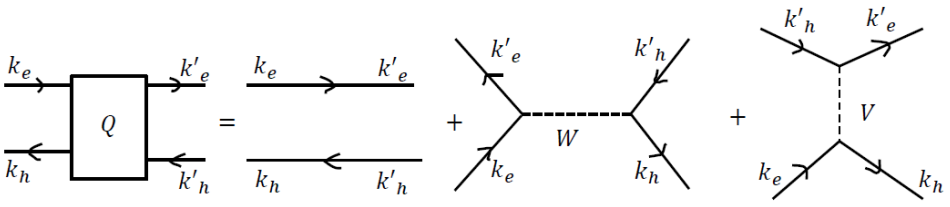

Figure 3.4: Correlated electron-hole pair with total momentum Q. The electron-hole kernel consist of the direct (W) and exchnage (V) terms. The direct term is computed with the screened Coulomb interaction as indicated with the solid dashed line, while the exchange term is calculated with the unscreened Coulomb interaction as indicated with the light dashed line.

where $\Delta_{cv}(\mathbf{k}_e, \mathbf{k}_h) = E_{c\mathbf{k}_e} - E_{v\mathbf{k}_h}$ is the quasi particle energy for a noninteracting electron-hole pair [8, 9] and Ω_n the exciton energy for the n^{th} excitation. The kernel $K(c\mathbf{k}_e, v\mathbf{k}_h; c\mathbf{k}'_e, v\mathbf{k}'_h)$ describes the interaction between all possible electron-hole pairs and it is given by

$$K(c\mathbf{k}_e, v\mathbf{k}_h; c\mathbf{k}'_e, v\mathbf{k}'_h) = 2\delta_S K^x(c\mathbf{k}_e, v\mathbf{k}_h; c\mathbf{k}'_e, v\mathbf{k}'_h) - K^d(c\mathbf{k}_e, v\mathbf{k}_h; c\mathbf{k}'_e, v\mathbf{k}'_h) \quad (3.21)$$

with $\delta_S = 1$ for spin singlet and 0 for spin triplet states. The direct (K^d) and exchange (K^x) terms are given by the following integrals:

$$\begin{aligned} K^d(c\mathbf{k}_e, v\mathbf{k}_h; c\mathbf{k}'_e, v\mathbf{k}'_h) &= \int \psi^*_{c\mathbf{k}'_e}(\mathbf{r})\psi_{v\mathbf{k}'_h}(\mathbf{r}')w(\mathbf{r}, \mathbf{r}')\psi^*_{v\mathbf{k}_h}(\mathbf{r}')\psi_{c\mathbf{k}_e}(\mathbf{r})\, d\mathbf{r}d\mathbf{r}' \\ K^x(c\mathbf{k}_e, v\mathbf{k}_h; c\mathbf{k}'_e, v\mathbf{k}'_h) &= \int \psi^*_{c\mathbf{k}'_e}(\mathbf{r})\psi_{v\mathbf{k}'_h}(\mathbf{r})v(\mathbf{r}, \mathbf{r}')\psi^*_{v\mathbf{k}_h}(\mathbf{r}')\psi_{c\mathbf{k}_e}(\mathbf{r}')\, d\mathbf{r}d\mathbf{r}' \end{aligned} \quad (3.22)$$

with w and v the screened and unscreened Coulomb potentials, respectively, and ψ is the quasiparticle wave function. We use the static dielectric constant approximation (see Eq. 3.12) to model the screened Coulomb potential ws and the Ohno

potential instead of v (see Eq. 3.13). Clearly, as the electron-hole interactions are screened, excitonic effects will be predominant whenever screening is weak, namely, in semiconducting tubes. Further, the binding energy is expected to be large in small tubes where holes and electrons are spatially confined.

3.3 Bright and dark exciton transformation and finite Q solution of the BS equation

In Fig. (3.5), we show plot the Brillouin zone of a zigzag SWNT showing the cutting lines corresponding to the μ-quantization and the K and K' points.

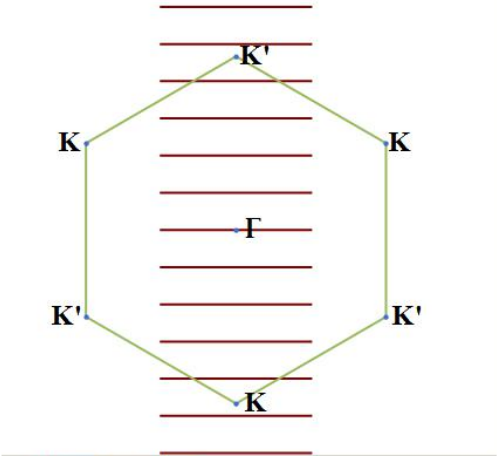

Figure 3.5: Brillouin zone of a zigzag SWNT showing cutting lines.

In what follows, we restrict our treatment only to excitons with zero angular momentum ($M = \mu_e - \mu_h = 0$). From the picture above, we can form the following electron-hole pair combinations at the K and K' points.

3.3.1 Electron-hole pair combinations at K point

The degenerate electron hole pair combinations together with their total momentum at the K point are given as

$$|\mu k_e; \mu k_h\rangle \quad (Q = k_e - k_h)$$

$$|\mu, -k_e; \mu, -k_h\rangle \quad (Q = k_h - k_e)$$

$$|\mu, k_e; \mu, -k_h\rangle \quad (Q = k_e + k_h)$$

$$|\mu, -k_e; \mu k_h\rangle \quad (Q = -k_e - k_h)$$

3.3.2 Electron-hole pair combinations at K' point

Similarly, the degenerate electron hole pair combinations together with their total momentum at the K' point are given as

$$|\bar{\mu} k_e; \bar{\mu} k_h\rangle \quad (Q = k_e - k_h)$$

$$|\bar{\mu}, -k_e; \bar{\mu}, -k_h\rangle \quad (Q = k_h - k_e)$$

$$|\bar{\mu}, k_e; \bar{\mu}, -k_h\rangle \quad (Q = k_e + k_h)$$

$$|\bar{\mu}, -k_e; \bar{\mu}, k_h\rangle \quad (Q = -k_e - k_h)$$

where $\bar{\mu}$ stands for $-\mu$. The only two states that have the same $Q = k_e - k_h$ are the states $|\mu k_e; \mu k_h\rangle$ and $|\bar{\mu}, k_e; \bar{\mu}, k_h\rangle$. The bright (+) and dark (-) single-particle combinations can thus be written as

$$\psi_{\pm}(\mathbf{r_e}, \mathbf{r_h}) = \frac{\psi_{c\mu k_e}(\mathbf{r_e})\psi^*_{v\mu k_h}(\mathbf{r_h}) \pm \psi_{c\bar{\mu} k_e}(\mathbf{r_e})\psi^*_{v\bar{\mu} k_h}(\mathbf{r_h})}{\sqrt{2}} \tag{3.23}$$

If we now introduce the new variables k (twice the relative momentum) and Q (center of mass momentum) such that

$$k_e = k + Q, \qquad k_h = k \tag{3.24}$$

then we can rewrite the bright and dark single-particle combinations (3.23) as

$$\psi_{\pm}(\mathbf{r_e}, \mathbf{r_h}) = \frac{1}{\sqrt{2}}\left[\psi_{c\mu k+Q}(\mathbf{r_e})\psi^*_{v\mu k}(\mathbf{r_h}) \pm \psi_{c\bar{\mu} k+Q}(\mathbf{r_e})\psi^*_{v\bar{\mu} k}(\mathbf{r_h})\right] \tag{3.25}$$

Under this transformation, the BS equation becomes diagonal in the subspace of bright and dark states. We can then solve for the bright and dark excitons independently. The generalized finite Q BS equation for $\alpha = (B, D)$ becomes

$$\Delta_Q(k)A^{(n)}_{\alpha,Q}(k) + \sum_{k'} K_{\alpha,Q}(k,k')A^{(n)}_{\alpha,Q}(k') = \Omega^{(n)}_{\alpha}(Q)A^{(n)}_{\alpha,Q}(k) \tag{3.26}$$

where

$$\Delta_Q(k) = E_{c\mu k+Q} - E_{v\mu k}$$

The transformed electron-hole kernel for the bright (B) exciton is

$$K_{B,Q}(k,k') = 4K^x_Q(k,k') - K^{d_1}_Q(k,k') - K^{d_2}_Q(k,k') \tag{3.27}$$

while that for the dark (D) exciton is

$$K_{D,Q}(k,k') = -K^{d_1}_Q(k,k') + K^{d_2}_Q(k,k') \tag{3.28}$$

where K^x_Q is the exchange matrix element, $K^{d_1}_Q$ is the Coulomb direct intra valley matrix element, and $K^{d_1}_Q$ the direct inter valley matrix element as discussed bellow. We remark immediately that for the dark excitons, there is no exchange interaction because the exchange interaction is the same for both intra and inter valley scattering processes.

3.3.3 Evaluation of Coulomb matrix elements

For the discrete lattice, the coulomb matrix elements can easily be evaluated. The direct intra valley matrix element is

$$K^{d_1}_Q(k,k') = \sum_{s,s'} C^{c*}_{\mu k+Q}(s)C^{v}_{\mu k}(s')w_{s,s'}(0,k'-k)C^{c}_{\mu k'+Q}(s)C^{v*}_{\mu k'}(s') \tag{3.29}$$

where

$$w_{s,s'}(\Delta\mu,\Delta q) \;=\; \frac{v_{s,s'}(\Delta\mu,\Delta q)}{\epsilon} \tag{3.30}$$

The direct inter valley matrix element is

$$K^{d_2}_Q(k,k') = \sum_{s,s'} C^{c*}_{\mu k+Q}(s)C^{v}_{\mu k}(s')w_{s,s'}(-2\mu,k'-k)C^{c}_{\bar{\mu} k'+Q}(s)C^{v*}_{\bar{\mu} k'}(s') \tag{3.31}$$

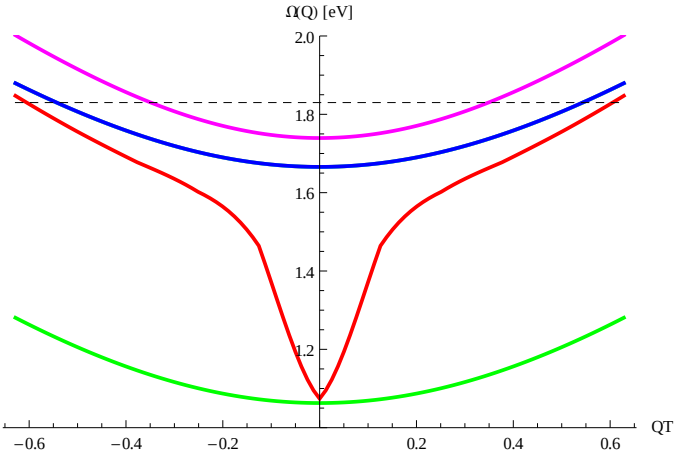

Figure 3.6: Excitation energy dispersions for the E_{11} excitons for an (11,0) SWNT plotted as a function of the dimensionless quantity QT where $T = 0.43$ nm is the translational periodicity: (Green) is for dark exciton $n = 1$ state; (Red) is for the lowest bright state; (Blue) is for the first excited dark state; and (Pink) for the first excited bright state. The dashed line indicates the position of the E_{11} band edge.

The exchange matrix element is the same for both intra and inter valley scattering processes and is given by

$$K_Q^x(k,k') = \sum_{s,s'} C^{c*}_{\mu k+Q}(s) C^{v}_{\mu k}(s) v_{s,s'}(0,Q) C^{c}_{\mu k'+Q}(s') C^{v*}_{\mu k'}(s') \tag{3.32}$$

The potential $w_{s,s'}(\Delta\mu, \Delta q)$ is the Fourier transform of the Coulomb interaction as given in Eq. (3.10).

3.4 Exciton dispersion, binding energy and wave function

The exciton dispersion $\Omega_\alpha^{(n)}(Q)$ is plotted for $n = 1, 2$ for the lowest bright (B) and dark (D) E_{11} excitons in Fig. (3.6). The dashed line in the figure indicates the position of the E_{11} band edge. The binding energy for the bright excitons is given

tube	$d_t(nm)$	r	E_g^0 [eV]	E_g [eV]	$\Omega_B^{(1)}(0)$ [eV]	E_b [eV]
(7,0)	0.55	2	1.43	3.39	2.39	1.00
(8,0)	0.63	1	1.36	2.53	1.50	1.03
(10,0)	0.79	2	1.02	2.62	1.87	0.75
(11,0)	0.87	1	0.98	1.83	1.07	0.76
(13,0)	1.03	2	0.79	2.17	1.57	0.60
(17,0)	1.35	1	0.63	1.14	0.64	0.50
(19,0)	1.51	2	0.54	1.66	1.24	0.42

Table 3.2: Renormalized band gap and exciton binding energies for different families $r = \mathrm{Mod}(2\mathrm{n} + \mathrm{m}, 3)$ of (n,0) tubes: E_g^0 is the bare band gap calculated using a π-orbital only TB model, E_g is the renormalized band gap, $\Omega_B^{(1)}(0)$ is the ground state excitation energy for the bright excitons, and E_b the exciton binding energy.

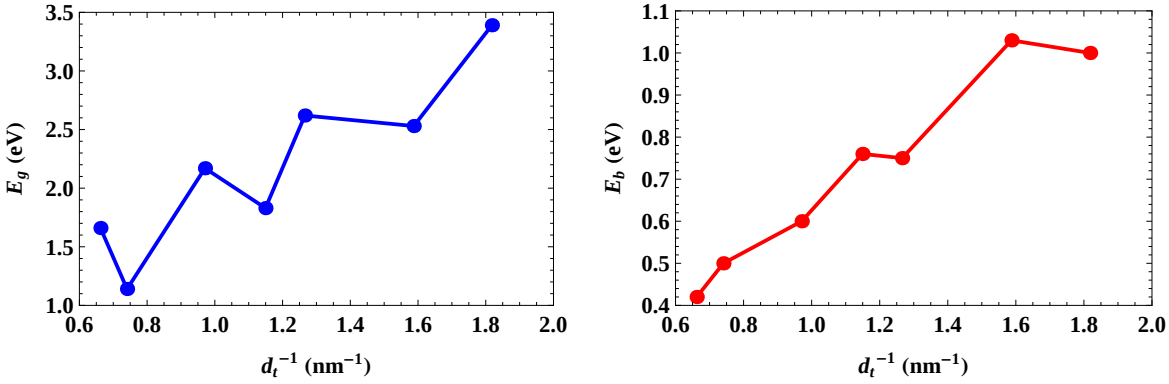

Figure 3.7: (Left panel) Renormalized band gap. (Right panel) Exciton binding energy.

by

$$E_b = E_g - \Omega_B^{(1)}(0) \tag{3.33}$$

where $\Omega_\alpha^{(1)}(0)$ is the ground state excitation energy of the exciton. The renormalized band gap and exciton binding energies for some zigzag tubes are shown in Table 3.2. The wave function of an exciton can now be expressed as linear combination

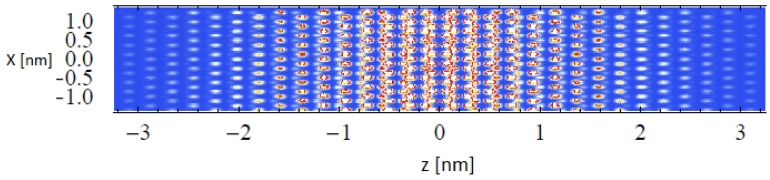

(a)

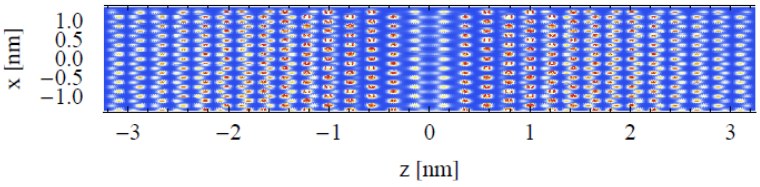

(b)

Figure 3.8: Exciton probability distribution $|\Psi^0(\mathbf{r}_e, \mathbf{r}_h)|^2$ for an (11,0) SWNT which gives the probability of finding an electron with the hole fixed at the origin (z is the tube axis and x is the circumferential direction) : (a) lowest bright state, and (b) first excited state.

of single-particle electron-hole pairs with the appropriate coupling coefficients as

$$\Phi^{(n)}_{\alpha,Q}(\mathbf{r}_e, \mathbf{r}_h) = \sum_k A^{(n)}_{\alpha,Q}(k) \Big[\psi_{c\mu k+Q}(\mathbf{r}_e)\psi^*_{v\mu k}(\mathbf{r}_h) + \\ +(-1)^s \psi_{c\bar{\mu} k+Q}(\mathbf{r}_e)\psi^*_{v\bar{\mu} k}(\mathbf{r}_h) \Big] \tag{3.34}$$

where $s = 0$ (1) corresponds to the bright (dark) state and the functions $\psi_{c\mu k}(\mathbf{r})$ are Bloch functions as defined in Eq. (2.14), and $\bar{\mu}$ stands for $-\mu$. Here, $A^{(n)}_{\alpha,Q}(k)$ is the exciton wave function in reciprocal space, which is obtained by solving the BS equation (3.20). We plot the exciton probability distribution $|\Phi^n_{B,0}(\mathbf{r}_e, \mathbf{r}_h)|^2$ (for $Q = 0$) for the bright excitons by fixing the position of the hole: Fig. 3.8 (a) shows

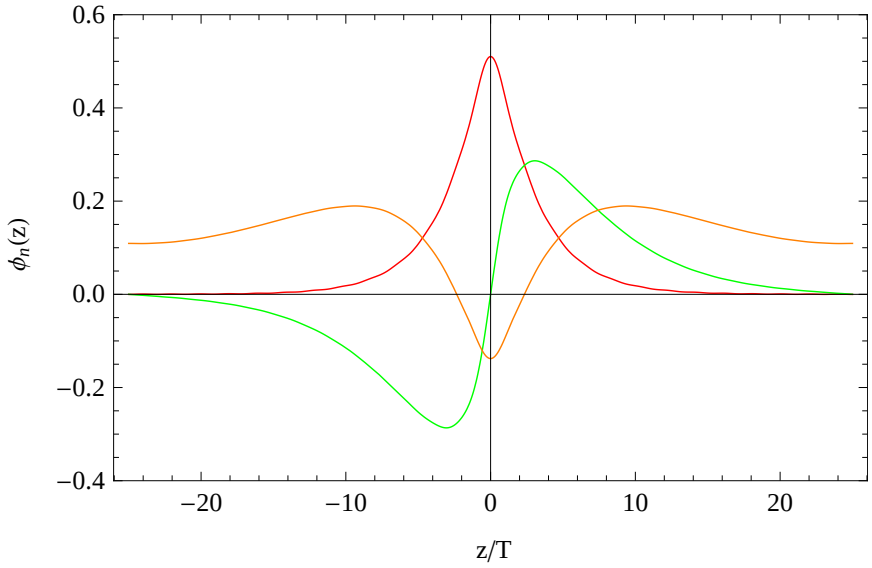

Figure 3.9: The real space exciton wave functions $\phi_n(z)$ for the three lowest $E_{11}(A)$ excitations for an (11,0) SWNT: (Red) is for the ground state $n = 1$; (Green) for the first excited state $n = 2$; and (Orange) for the second excited state $n = 3$. $\phi_n(z)$ is related to the dipole of distribution of the exciton along the axial direction.

the bright exciton for an (11,0) SWNT. The exciton is localized in the direction of the tube axis, z, but delocalized along the tube circumference, x. Fig. 3.8 (b) shows the probability distribution for the first excited state for the bright exciton. For this state, the probability of finding the electron and hole to be on same position is very small. This behavior is in agreement with variational calculations [24].

To study the variation of the exciton wave function along the tube axis, we plot the quantity

$$\phi_n(z_e - z_h) = \sum_k A^{(n)}_{B,0}(k) e^{ik(z_e - z_h)} \tag{3.35}$$

which is the exciton probability amplitude along the tube axis. In Fig. 3.9 we show the exciton envelop wave functions $\phi_n(z)$ for the three lowest $E_{11}(A^n_B)$ $(n = 1, 2, 3)$ excitons. From the $E_{11}(A^0_B)$ to the $E_{11}(A^2_B)$ state, the excitation energy increases and the wave function delocalizes. For an achiral (armchair or zigzag) SWNT, exciton wave functions are either even or odd functions of the relative coordinate

z because of the inversion symmetry of the SWNT lattice. $E_{11}(A_B^1)$ and $E_{11}(A_B^3)$ states are symmetric states and the $E_{11}(A_B^1)$ state is an antisymmetric state. It follows that $E_{11}(A_B^1)$ and $E_{11}(A_B^3)$ excitons are bright and the $E_{11}(A_B^2)$ is dark with respect to parallel polarized light ($\mathcal{E} \parallel z$).

For the ground state, we can show that the wave function along the tube axis can be expressed as a Gaussian envelop function:

$$\phi_1(z_e - z_h) \propto e^{-(z_e - z_h)^2/2a_B^2} \tag{3.36}$$

where a_B is the electron-hole correlation length (exciton Bohr radius). For an (11,0) SWNT as shown in Fig. 3.9, $a_B \approx 6T = 2.58$ nm.

3.5 Summary

In this chapter, we have examined the crucial role that Coulomb effects play in the electronic properties of SWNTs. We have seen that enhanced Coulomb interactions in quasi-1D systems like carbon nanotubes lead to band gap renormalization and the formation of strongl bound excitons. We calculated the renormalized band gap for different nanotubes placed in different dielectric media. We show that the renormalized band gap can be a significant fraction of the free particle band gap and exhibits a strong family pattern. We elucidated the role of the physical environment by calculating the band gap as a function of the environmental screening parameter ϵ. Further, we reviewed the theory of excitons in carbon nanotubes and calculated exciton dispersion and binding energy for selected tubes. The wave functions of the photogenerated correlated electron-hole pairs are spread over the circumference of the nanotube. The large electron-hole overlap results in a strongly bound exciton that can move freely along the tube, with a binding energy typically of the order of several tenths of an electron volt.

In the next chapter, we shall investigate the extrinsic properties of carbon nanotubes doped with charged impurity atoms. We will formulate the impurity problem for low dimensional systems like carbon nanotubes.

Chapter 4

Theory of interaction of excitons with charged impurities

In this chapter, we develop a model for studying the interaction of bright excitons in semiconducting single-wall nanotubes with charged impurities. The model reveals red shift in the energy of excitonic states in the presence of impurity, thus indicating binding of free excitons in the impurity potential well. Several bound states were found in the absorption spectrum below the onset of excitonic optical transitions in the bare nanotube. Dependence of the binding energy on the model parameters, such as impurity charge and position, was determined and analytical fits were derived for a number of tubes of different diameter. The nanotube family splitting is seen in the diameter dependence, gradually decreasing with the diameter.

4.1 Introduction

As quasi-1D systems, SWNTs are highly sensitive to the surrounding environment. The large influence of the physical environment on excited states of SWNTs makes them good candidates for sensitive nanoscale detectors [19, 69–71]. The

functionalization of nanotubes enables the control and optimization of their properties and is a promising strategy to exploit their tremendous application potential [72–74]. The effect of the carbon nanotube outer environment has been studied intensively [15, 75–79]. Additionally, it has been observed that the inner environment (for example water-filling) can also influence the photoluminescence (PL) of SWNTs. Redshifts in the PL spectra upon water filling [80], can be used to unambiguously distinguish empty SWNTs from filled ones. Most recently the focus of research was on the interactions of excitons with a single charge of mobile (or localized) electron/hole (thus forming a mobile or localized three-body trion) and exciton interactions with point charge impurity ions [41–44, 81]. The functionalization of carbon nanotubes with single atoms or molecules is quite different from solvent functionalization (common solvatochromism) which has been studied widely, and is known to produce redshifts in the optical excitations of a nanotube [59–61]. Recent theoretical studies have been conducted in which the environment (here, a single atom or molecule or another nanotube) has been treated more elaborately. For instance, Y. Tomio et al, have examined the effects of screening by the interwall Coulomb interaction on excitons and optical spectra in double-wall tubes based on the effective-mass theory and a static screened Hartree-Fock approximation [82]. Moreover, E. Malic et al have applied the formalism of density matrix theory to describe the optical and electronic properties of carbon nanotubes functionalized with noncovalently adsorbed spiropyran molecules [49]. Furthermore, M. Rohlfing has applied many-body perturbation theory to study redshift of excitons in carbon nanotubes caused by environmental polarizability (here, due to another SWNT or nitrogen molecule) [83].

In order to further investigate the functionalization with single charged molecules or atoms absorbed on the surface of a nanotube, we consider the interaction of a SWNT with a single immobile charged impurity. We treat the physical environment (here, single immobile charged impurity) more elaborately, thus going beyond previous studies in which the SWNTs were considered in vacuum or immersed in ionic polymer or surfactant [58–60]. We formulate the problem using many-body perturbation theory within the TBA, thus providing a very simple, but computationally

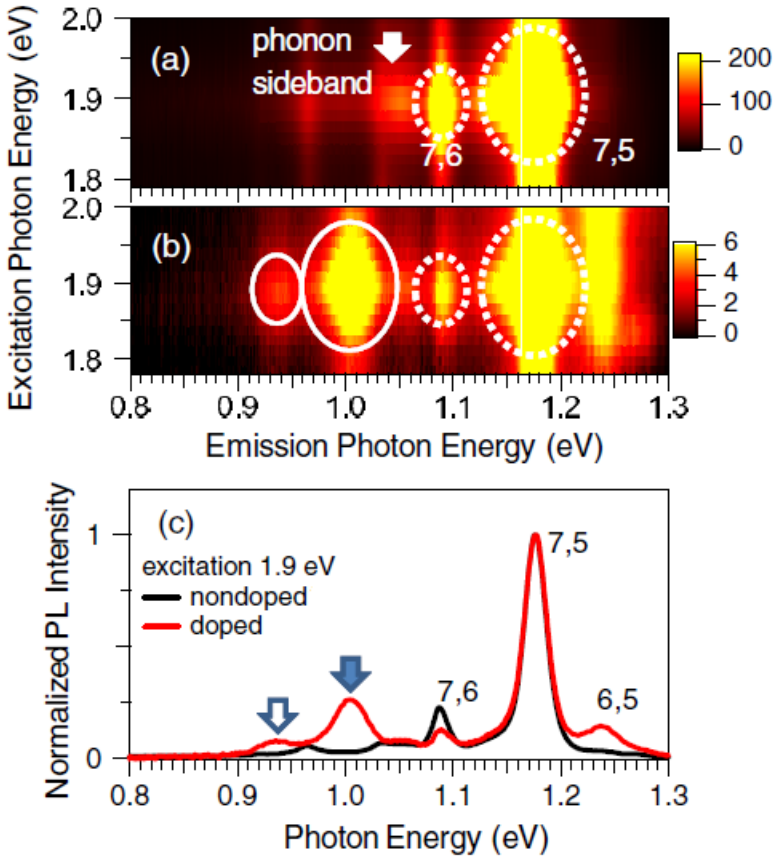

Figure 4.1: R. Matsunaga et al [42]: Photoluminescence excitation (PLE) contour maps of (a) nondoped nanotubes, (b) doped nanotubes . The dotted circles show the E_{11} bright excitons and the solid circles show the new PL peaks due to hole doping. (c) The normalized PL spectra of the nondoped and doped nanotubes [from (a) and (b), respectively] at the excitation photon energy of 1.9 eV. The doping-induced new PL peaks of (7,5) and (7,6) nanotubes are indicated by the solid and open arrows, respectively.

very efficient means to study these effects.

4.2 Experimental results on interaction of excitons with charged impurities

From an experimental point of view, the investigation of the optical properties of nanotubes has shifted from pristine SWNTs tubes toward the extrinsic effects (due to adatoms or molecules). More specifically, the optical properties of carbon nanotubes doped with impurities has received much attention. Many optical measurements have been performed with hole doped nanotubes, revealing the formation of many-body bound states (charged excitons or trions) in carbon nanotubes [41–44, 84]. In particular, R. Matsunaga et al recently reported the existence of a new excited state below the lowest (E_{11}) singlet exciton state in hole doped single-walled carbon nanotubes [42]. As shown in Fig. 4.1, in both PL and absorption spectroscopy, a new peak appears with hole doping at room temperature, regardless of the dopant species. This PL peak is attributed to the formation of trions.

In what follows, we present a theoretical formalism of the problem of interaction of exciton with an immobile charged impurity. Later, we shall discuss the details of the procedure and then present some results.

4.3 General formalism

The impurity problem plays a great role in solid state physics. Selected impurities are frequently introduced into semiconductors to produce n-type or p-type doping. The introduction of impurities into a crystal lattice results in a perturbation to the periodic potential giving rise to bound impurity levels. Any disturbance to the periodic potential results in energy levels different from the energy levels of the perfect crystal. In this work, we formulate a theory for the interaction of a single charged impurity with optical excitations (excitons) of semiconducting SWNTs.

We consider a SWNT of finite length L and radius R, whose excitations are dominated by correlated electron-hole pairs (excitons), interacting with an impurity ion with effective charge $Z|e|$ (Z being the effective valency of the ion) placed at a

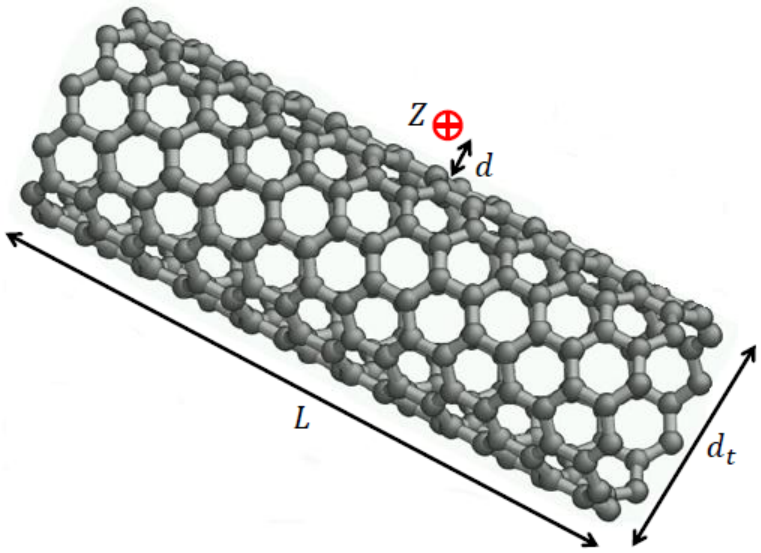

Figure 4.2: Schematic representation of the system of a SWNT interacting with a charged impurity. For a given tube with the length, L, and diameter, d_t, the model parameters include the effective charge of the impurity ion, Z, and the position of the ion, $\mathbf{r_p}$.

distance d above the surface of the SWNT, as shown in Fig. 4.2. In our model, we treat the impurity ion as a perturbation to the excitons in the pristine SWNT. That is, we assume that the polarization of the single-particle electron and hole states of the pristine SWNT due to impurity ion is negligible so one can use the same single-particle wave functions even in the presence of the impurity. The explicit form of the single-particle wave function is (see Eq. 2.14):

$$\psi_{\lambda\mu k}(\mathbf{r}) = \sum_{s=1}^{4} C_{\mu k}^{\lambda}(s)\psi_{sk}(\mathbf{r}), \quad \lambda = c, v \tag{4.1}$$

The total two-body Hamiltonian of the system, including perturbation, may be expressed as [85]

$$H = H_{BS} + H_{int} \tag{4.2}$$

where $H_{BS} = D + 2K_x - K_d$ is the bare BS Hamiltonian, which has translational symmetry of the SWNT lattice. The diagonal term of the BS Hamiltonian, $D =$

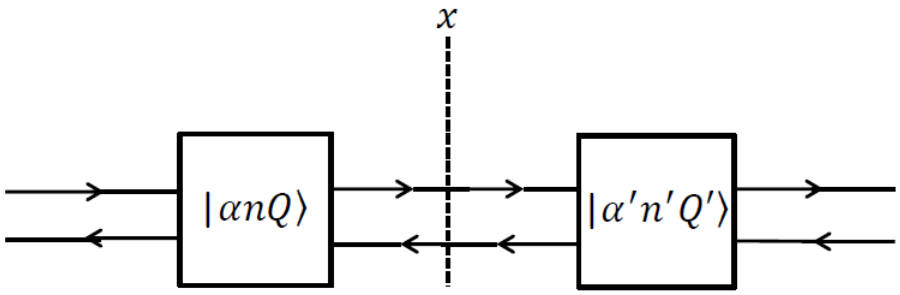

Figure 4.3: Schematic representation of the interaction between exciton and impurity .

$E_c - E_v$, is the sum of the quasiparticle energies for the uncorrelated electron-hole pair, where K_x and K_d are the exchange and direct Coulomb interaction [66–68].

The operator of interaction with the ion is:

$$H_{int}(\mathbf{r}_e, \mathbf{r}_h) = \frac{Ze^2}{|\mathbf{r}_h - \mathbf{r_p}|} - \frac{Ze^2}{|\mathbf{r}_e - \mathbf{r_p}|} \tag{4.3}$$

here $\mathbf{r}_e$ and $\mathbf{r}_h$ refer to the position vector of the electron and hole, respectively; while $\mathbf{r_p}$ refer to the position of the impurity ion. Since the interaction potential includes both electron and hole symmetrically and we also assume electron-hole symmetry in single-particle band structure, the model gives the same magnitude of perturbation for both positively and negatively charged impurity. Furthermore, in the second order of perturbation theory implemented below, the exciton binding is the same for either sign of the ion charge. (One can part the assumption of electron-hole symmetry and use the same model, to be discussed elsewhere, although some of the simplifications presented below will not be possible then.) It is more convenient to solve Eq.(4.2) in momentum space: then the BS Hamiltonian can be written as [66]

$$H_{BS} A^{(n)}_{\alpha,Q}(k) = \Omega^{(n)}_{\alpha}(Q) A^{(n)}_{\alpha,Q}(k) \tag{4.4}$$

here $\Omega^{(n)}_{\alpha}(Q)$ is the energy of the nth excitation, α is the quantum number distinguishing bright (B) and dark (D) excitons, Q is the center of mass momentum, and

$A^{(n)}_{\alpha,Q}(k)$ is the excitonic wave function in the momentum representation. We consider only excitons with zero total angular momentum. In the coordinate space the exciton wave function, the solution of the bare BS Hamiltonian, can be expressed as a linear combination of the single-particle electron-hole pairs (see Eq. 3.34):

$$\begin{aligned}\Phi^{(n)}_{\alpha,Q}(\mathbf{r}_e,\mathbf{r}_h) &= \sum_k A^{(n)}_{\alpha,Q}(k)\Big[\psi_{c\mu k+Q}(\mathbf{r}_e)\psi^*_{v\mu k}(\mathbf{r}_h) + \\ &\quad +(-1)^s\psi_{c\bar{\mu}k+Q}(\mathbf{r}_e)\psi^*_{v\bar{\mu}k}(\mathbf{r}_h)\Big] \qquad (4.5)\end{aligned}$$

here $s = 0/1$ corresponds to the bright/dark state and the functions $\psi_{c\mu k}(\mathbf{r})$ are single-particle wave functions.

In the presence of the impurity, one has to solve the scattering problem. The scattered state can be expressed as

$$\Psi^{(i)}(\mathbf{r}_e,\mathbf{r}_h) = \sum_{n\alpha Q} \mathcal{C}^{(i)}_{\alpha nQ}\Phi^{(n)}_{\alpha,Q}(\mathbf{r}_e,\mathbf{r}_h) \qquad (4.6)$$

where the wave function amplitudes $\mathcal{C}^{(i)}_{\alpha nQ}$ must satisfy Eq.(4.2). In the momentum space it reads as:

$$\Big[\Omega^{(n')}_{\alpha'}(Q')\delta_{nn'}\delta_{\alpha\alpha'}\delta_{QQ'} + S^{nn'}_{\alpha,\alpha'}(Q,Q')\Big]\mathcal{C}^{(i)}_{\alpha' n'Q'} = E^{(i)}\mathcal{C}^{(i)}_{\alpha nQ} \qquad (4.7)$$

with the matrix elements $S^{nn'}_{\alpha,\alpha'}(Q,Q')$ given by

$$\begin{aligned}S^{nm}_{\alpha,\alpha'}(Q,Q') &= \langle\Phi^{(n)}_{\alpha,Q}|H_{int}|\Phi^{(m)}_{\alpha',Q'}\rangle \\ &= \int d\mathbf{r}_e d\mathbf{r}_h \Phi^{(n)*}_{\alpha,Q}(\mathbf{r}_e,\mathbf{r}_h)H_{int}(\mathbf{r}_e,\mathbf{r}_h)\Phi^{(m)}_{\alpha',Q'}(\mathbf{r}_e,\mathbf{r}_h) \qquad (4.8)\end{aligned}$$

We illustrate the scattering process of an exciton by an impurity atom in Fig. 4.3. In principle, the eigenstates, labeled with the new quantum number i, represent scattered states of perturbed continuum as well as bound states, localized near the impurity as we will show below.

The impurity binding energy for the ith scattered state, $I^{(i)}_E$, is defined as the difference with the energy level of the lowest state of unperturbed bright exciton ($n = 1$):

$$I^{(i)}_E = E^{(i)} - \Omega^{(1)}_B(0) \qquad (4.9)$$

In what follows, we focus on the binding energy of the lowest scattered state ($i = 1$) and for shortcut notations we use below: $I_E \equiv I_E^{(1)}$.

4.4 Evaluation of matrix elements and detailed derivation of the coupling between bright and dark excitons

For excitons with zero total angular momentum, the Hilbert space of solutions of the BS equation consist of the bright and dark subspaces: $|B\rangle$ and $|D\rangle$. We do not consider K-excitons here. Then the impurity Hamiltonian (Eq. 4.2) obtains the form

$$H = \begin{pmatrix} \Omega_B + S_{BB} & S_{BD} \\ S_{DB} & \Omega_D + S_{DD} \end{pmatrix} \tag{4.10}$$

The coupling between bright and dark excitons of total angular momentum zero is described by the matrix element $S^{nm}_{B,D}(Q, Q')$ which may be expressed as

$$S^{(nm)}_{B,D}(Q, Q') = \sum_{k,k'} A^{*(n)}_{B,Q}(k) A^{(m)}_{D,Q'}(k') \Big[G_{KK} - G_{KK'} + G_{K'K} - G_{K'K'} \Big] \tag{4.11}$$

where

$$\begin{aligned}
G_{KK} &= \int d\mathbf{r}_e d\mathbf{r}_h \psi^*_{c\mu k+Q}(\mathbf{r}_e) \psi_{v\mu k}(\mathbf{r}_h) H_{int}(\mathbf{r}_e, \mathbf{r}_h) \psi_{c\mu k'+Q'}(\mathbf{r}_e) \psi^*_{v\mu k'}(\mathbf{r}_h) \\
G_{K'K'} &= \int d\mathbf{r}_e d\mathbf{r}_h \psi^*_{c\bar{\mu} k+Q}(\mathbf{r}_e) \psi_{v\bar{\mu} k}(\mathbf{r}_h) H_{int}(\mathbf{r}_e, \mathbf{r}_h) \psi_{c\bar{\mu} k'+Q'}(\mathbf{r}_e) \psi^*_{v\bar{\mu} k'}(\mathbf{r}_h) \\
G_{KK'} &= \int d\mathbf{r}_e d\mathbf{r}_h \psi^*_{c\mu k+Q}(\mathbf{r}_e) \psi_{v\mu k}(\mathbf{r}_h) H_{int}(\mathbf{r}_e, \mathbf{r}_h) \psi_{c\bar{\mu} k'+Q'}(\mathbf{r}_e) \psi^*_{v\bar{\mu} k'}(\mathbf{r}_h) \\
G_{K'K} &= \int d\mathbf{r}_e d\mathbf{r}_h \psi^*_{c\bar{\mu} k+Q}(\mathbf{r}_e) \psi_{v\bar{\mu} k}(\mathbf{r}_h) H_{int}(\mathbf{r}_e, \mathbf{r}_h) \psi_{c\mu k'+Q'}(\mathbf{r}_e) \psi^*_{v\mu k'}(\mathbf{r}_h)
\end{aligned} \tag{4.12}$$

In semiconducting SWNTs, there are two degenerate valleys associated with the K and K' points at the corner of the first Brillouin zone, therefore all exciton-impurity

scattering states can be expressed in terms of the four G matrix elements. The problem of computing matrix elements like G_{KK} is greatly simplified because our interaction Hamiltonian can be expressed as the sum of two one-body potentials as

$$H_{int}(\mathbf{r}_e, \mathbf{r}_h) = H_h(\mathbf{r_h}) + H_e(\mathbf{r_e}) \tag{4.13}$$

where

$$H_h(\mathbf{r_h}) = \frac{Ze^2}{|\mathbf{r}_h - \mathbf{r_p}|}, \quad H_e(\mathbf{r_e}) = -\frac{Ze^2}{|\mathbf{r}_e - \mathbf{r_p}|} \tag{4.14}$$

Let us compute G_{KK} exactly. We have

$$\begin{aligned} G_{KK} &= \int d\mathbf{r}_e d\mathbf{r}_h \psi^*_{c\mu k+Q}(\mathbf{r}_e)\psi_{v\mu k}(\mathbf{r}_h)H_{int}(\mathbf{r}_e,\mathbf{r}_h)\psi_{c\mu k'+Q'}(\mathbf{r}_e)\psi^*_{v\mu k'}(\mathbf{r}_h) \\ &= \int d\mathbf{r}_h \psi_{v\mu k}(\mathbf{r_h})H_h(\mathbf{r_h})\psi^*_{v\mu k'}(\mathbf{r}_h) \times \\ &\quad \times \int d\mathbf{r}_e \psi^*_{c\mu k+Q}(\mathbf{r_e})\psi_{c\mu k'+Q'}(\mathbf{r}_e) + \\ &\quad - \int d\mathbf{r}_h \psi_{v\mu k}(\mathbf{r_h})\psi^*_{v\mu k'}(\mathbf{r}_h) \times \\ &\quad \times \int d\mathbf{r}_e \psi^*_{c\mu k+Q}(\mathbf{r_e})H_e(\mathbf{r_e})\psi_{c\mu k'+Q'}(\mathbf{r}_e) \end{aligned} \tag{4.15}$$

If we neglect the polarization of the one-electron wave functions, then we can use the orthonormality condition of the Bloch functions

$$\int d\mathbf{r}\ \psi_{v\mu k}(\mathbf{r})\psi^*_{v\mu' k'}(\mathbf{r}) = \delta_{\mu,\mu'}\delta_{k,k'} \tag{4.16}$$

to simplify the above equation and finally obtain:

$$G_{KK} = I_h(Q, Q', k, k') - I_e(Q, Q', k, k') \tag{4.17}$$

where

$$\begin{aligned} I_h &= \delta_{k+Q,k'+Q'} \int d\mathbf{r}_h \psi_{v\mu k}(\mathbf{r_h})H_h(\mathbf{r_h})\psi^*_{v\mu k'}(\mathbf{r}_h) \\ I_e &= \delta_{k,k'} \int d\mathbf{r}_e \psi^*_{c\mu k+Q}(\mathbf{r_e})H_e(\mathbf{r_e})\psi_{c\mu k'+Q'}(\mathbf{r}_e) \end{aligned} \tag{4.18}$$

where

$$
\begin{aligned}
I_h &= \delta_{k+Q,k'+Q'} \int d\mathbf{r}_h \psi_{v\mu k}(\mathbf{r_h}) H_h(\mathbf{r_h}) \psi^*_{v\mu k'}(\mathbf{r}_h) \\
I_e &= \delta_{k,k'} \int d\mathbf{r}_e \psi^*_{c\mu k+Q}(\mathbf{r_e}) H_e(\mathbf{r_e}) \psi_{c\mu k'+Q'}(\mathbf{r}_e)
\end{aligned} \tag{4.19}
$$

We can proceed in a similar fashion to compute all the matrix elements $G_{K'K'}, G_{K,K'}$ and $G_{K',K}$. It is trivial to show that

$$
G_{K'K'} = G_{KK}, \quad G_{KK'} = G_{K'K} = 0 \tag{4.20}
$$

Therefore, this perturbation potential cannot mix the bright and dark states. This means that the Hamiltonian matrix is block-diagonal. For the bright exciton, for example, sought solutions should be obtained from the Hamiltonian:

$$
H_B = \Omega_B + S_{BB} \tag{4.21}
$$

while for a dark exciton from:

$$
H_D = \Omega_D + S_{DD} \tag{4.22}
$$

4.5 Numerical solution of the impurity scattering equation and discussion of the results

The task of solving Eq. (4.7) can be very formidable, however, a few approximations help us to reduce the computational burden. The interaction Hamiltonian does not couple the bright and dark excitons as derived in the previous section. Thus one can solve Eq. (4.7) separately for the bright and dark manifolds and $S^{nn'}_{\alpha,\alpha'}(Q,Q')$ is diagonal in α, α' indexes. Still, even in the subspace of bright states, the tensor $S^{nn'}_{BB}(Q,Q')$ can be very large since it includes a number of excitonic states with different Q and n quantum numbers.

In order to calculate the energy of the lowest state and I_E in the most efficient way we have to reduce the size of $S^{nn'}$ matrix. We compute $I_E(n)$ as a function

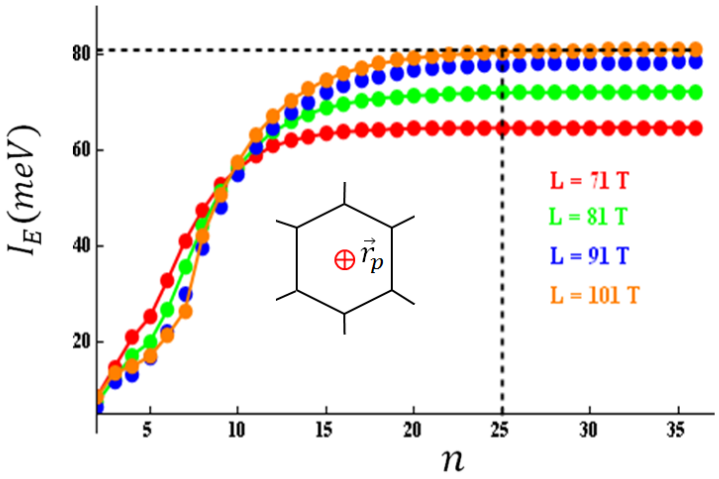

Figure 4.4: Convergence of the exciton binding energy, I_E, as a function of the number of included exciton bands, n, for different lengths of (11,0) SWNT computed for $d = 2$ Å and $Z = 3$, with the impurity position ($\mathbf{r_p}$) at the center of the hexagon: (red) $L = 71T$, (green) $L = 81T$, (blue) $L = 91T$, (orange) $L = 101T$, where $T = 0.43$ nm is the unit cell length.

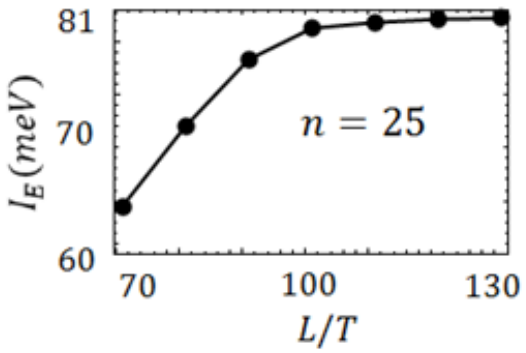

Figure 4.5: Convergence of the exciton binding energy with respect to SWNT length, L, for $n = 25$.

of the $n-$cut off, and increase n until we reach convergence, as illustrated in Fig. 4.4 for a (11,0) SWNT. Same convergence was obtained for $Q-$cut off. Since we performed our calculations for a finite length nanotube, we ensure the stability of

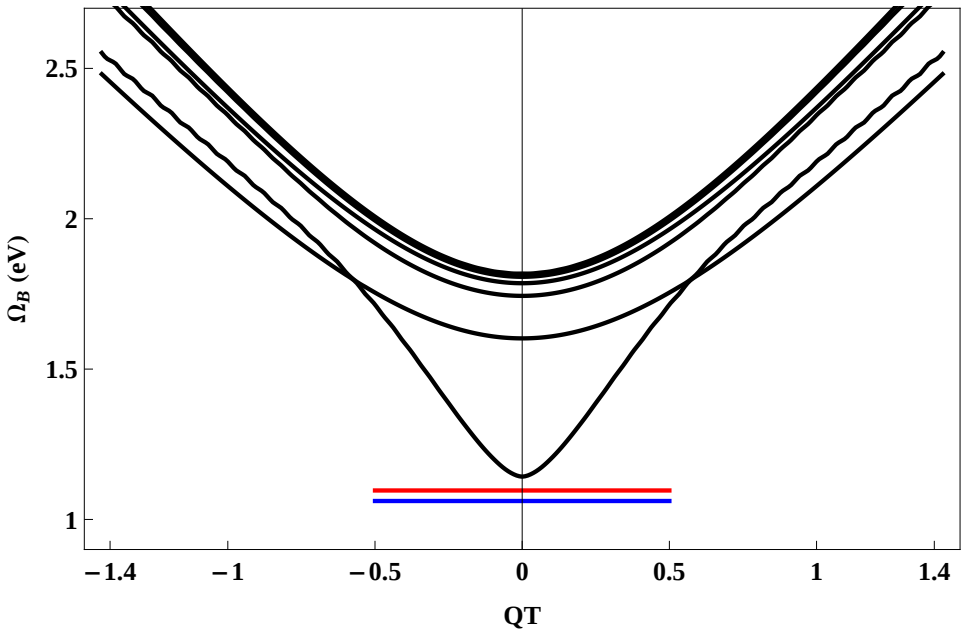

Figure 4.6: Exciton dispersion relation for an (11,0) SWNT plotted as a function of the dimensionless quantity QT, where $T = 0.43$ nm is the unit cell length. The two horizontal lines represent the localized states with binding energies $E_b = 81$ meV and $E_b = 46$ meV calculated for $d = 2$ Å and $Z = 3$.

numerical results with changing the length of the system (see Fig. 4.5). For this particular example of (11,0) SWNT a cut off length of $L = 101T$ (where $T = 0.43$ nm is the unit cell length) and a cut off number of bands of $n = 25$ allowed to achieve convergence for the exciton binding energy.

Fig. 4.6 shows the exciton dispersion for pristine (11,0) SWNT together with the impurity induced bound states with binding energies $E_b = 81$ meV and $E_b = 46$ meV calculated for $d = 3$ Å and $Z = 3$.

We found pronounced dependence of I_E on tube diameter, d_t. In Fig. 4.7, I_E is shown as a function of d_t. Data points branch into two curves for two different families $r = \mathrm{Mod}(2\mathrm{n} + \mathrm{m}, 3)$ of zigzag tubes. The family splitting however decreases with increasing d_t. This can be due to decreasing SWNT curvature or due to the overall dipole matrix element with respect to the ion position (above the SWNT surface) decreases with increasing the nanotube size. In order to further investigate

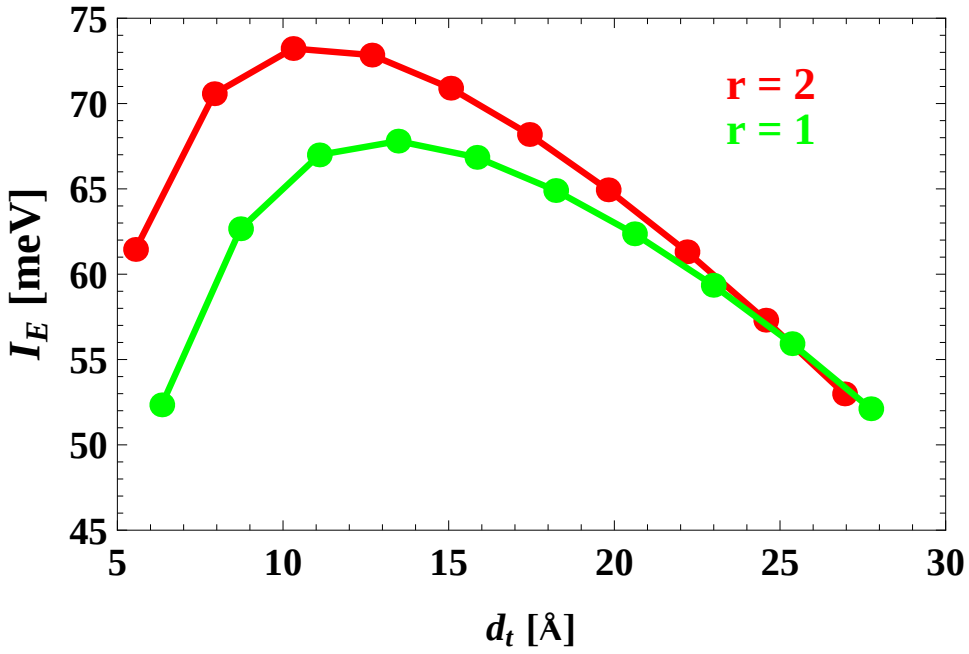

Figure 4.7: Impurity binding energy (I_E) as a function of tube diameter d_t for $Z = 3$ of impurity ion for $d = 3$ Å. Red and green points indicate zigzag tubes of different families.

this we performed detailed analysis of the behavior of I_E with varying position of the impurity (and also its charge) for the fixed value of d_t.

For a given SWNT, the interaction Hamiltonian H_{int} given by Eq.(4.3) depends parametrically on Z and $\mathbf{r}_p = ((R+d)\cos\theta, (R+d)\sin\theta, z)$. Dependence of I_E on these parameters is expected to be commensurate with the symmetry of the SWNT lattice.

Fig. 4.8 presents the variation of the exciton binding energy profile: $I_E(x, z)$, where $x = (R+d)\theta$ is the (curvilinear) surface coordinate in the circumferential direction, and z in the axial direction. The $I_E(x, z)$ profile, shown for (11,0) SWNT (within one unwrapped unit cell) for fixed $d = 3$Å and $Z = 3$, has the maximum when the impurity is right above the center of carbon bond, and the minimum above the center of the hexagon.

Now, we consider the dependence of I_E on d for fixed Z. Fig. 4.7 shows the

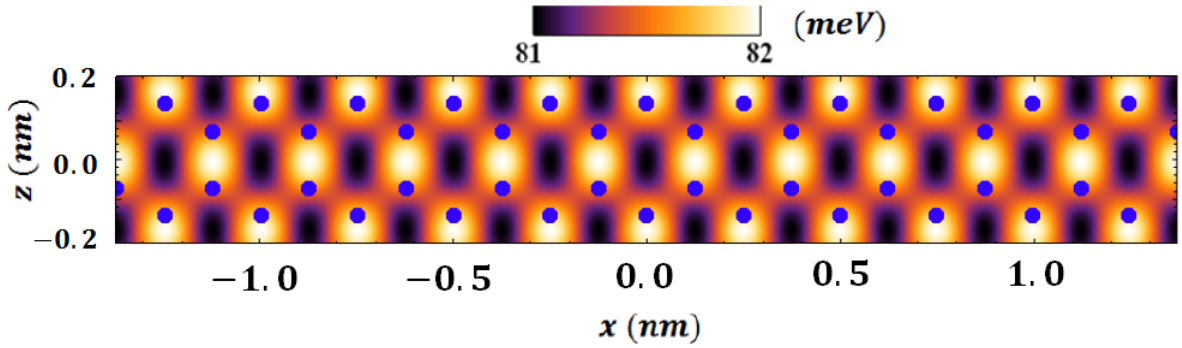

Figure 4.8: Impurity energy distribution for an (11,0) SWNT calculated for $d = 2$Åand $Z = 3$. It shows that the single impurity preserves the symmetries of the SWNT.

variation of I_E with d for (11,0) SWNT with the ion position shown in the inset of Fig. 4.4 and $Z = 3$. For small separation from the nanotube wall one can fit the dependence with the exponential function:

$$I_E(d) = I_0 \exp(-d/d_0) \tag{4.23}$$

where the amplitude, I_0, and the characteristic distance, d_0, vary with the tube diameter, and the effective valency Z. Just as we did for the impurity energy distribution, we can study the distribution of I_0 and d_0 within the unit cell. This can be done as follows: for each point (x, z) on the surface of the SWNT, we plot I_E as a function of d and use it to fit the quantities $I_0(x, z)$ and $d_0(x, z)$. We show in Fig. 4.9, the plots of $I_0(x, z)$ and $d_0(x, z)$. The two quantities are well correlated, when $I_0(x, z)$ is increasing, $d_0(x, z)$ is decreasing and vice-versa. We found the average value of I_0 and d_0 to be $I_0 = \langle I_0(x, z)\rangle = 219$ mev, and $d_0 = \langle d_0(x, z)\rangle = 2.33$ Å. A similar fitting procedure can be carried out for tubes with different diameters. Table 4.1 presents the fitting parameters for 6 zigzag SWNTs of different diameters (computed with the position of the impurity $\mathbf{r}_p$ in the center of the hexagon, as indicated in the inset of Fig. 4.4).

This exponential fit of the binding energy works well for the distances 2Å $\leq d \leq$ 20Å. Since the perturbation due to a single charged impurity is weak, this is the

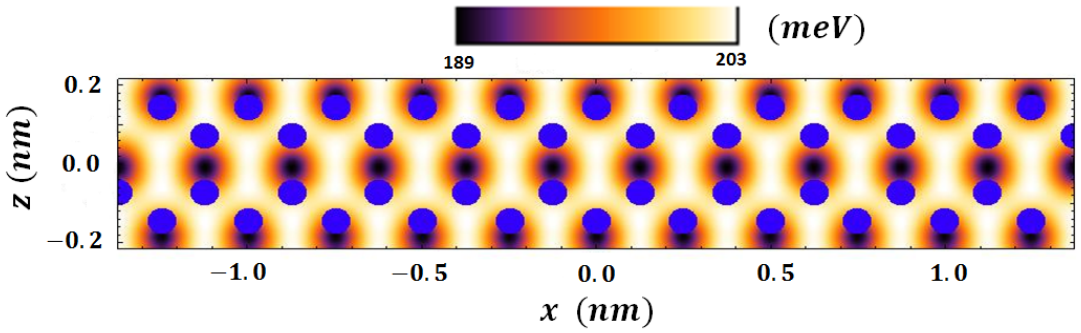

(a)

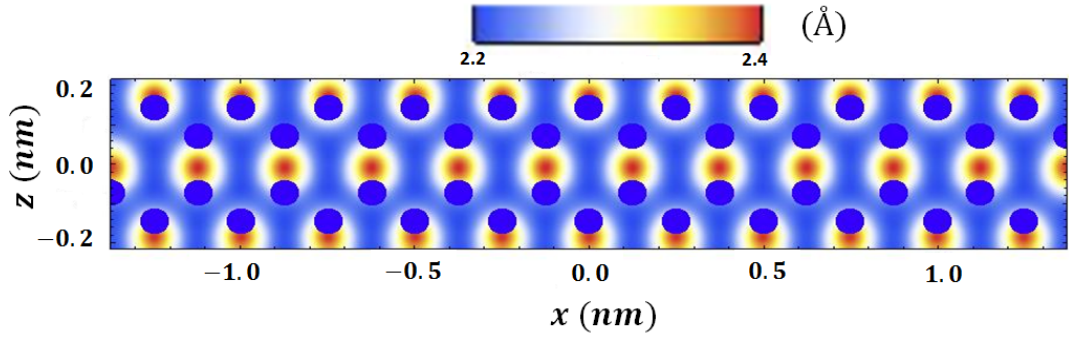

(b)

Figure 4.9: Distribution of the fitted parameters $I_0(x,z)$ and $d_0(x,z)$ for an (11,0) nanotube, computed using $Z = 3$: (a) shows the quantity $I_0(x,z)$; (b) is the plot of $d_0(x,z)$.

region of interest to be compared with the experiments. We remark however that for large distances the dipole approximation for the exciton becomes valid. In this approximation, the perturbation due to impurity may be expressed as

$$H_{int} = \frac{-e\mathbf{r} \cdot Ze(\mathbf{R}_{cm} - \mathbf{r_p})}{|\mathbf{R}_{cm} - \mathbf{r_p}|^3} \tag{4.24}$$

where $\mathbf{r} = \mathbf{r}_e - \mathbf{r_h}$ is the relative coordinate of the exciton, and $\mathbf{R}_{cm} = (\mathbf{r}_e + \mathbf{r_h})/2$

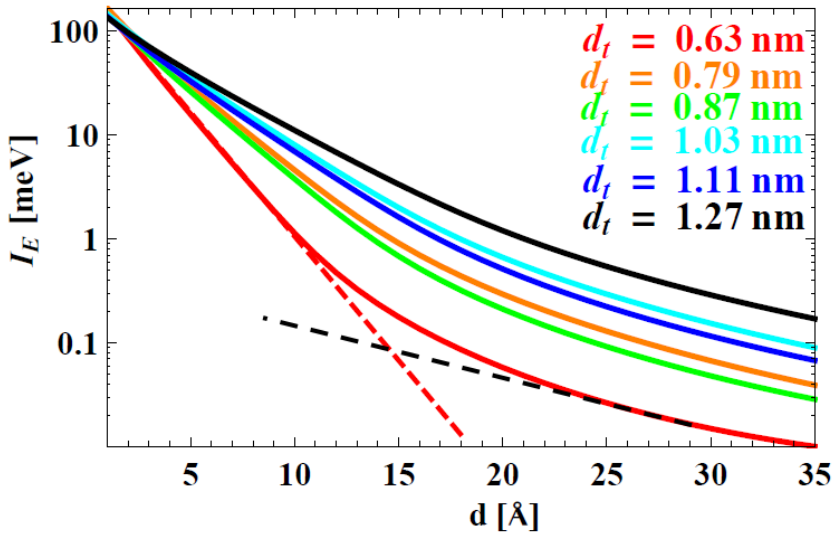

Figure 4.10: Exciton binding energy, I_E (log-scale), vs. distance to impurity, d, for few $(n,0)$ SWNTs and $Z=3$: (red) is for (8,0) tube; (orange) for (10,0) tube; (green) for (11,0); (cyan) for (13,0); (blue) for (14,0); and (black) for (16,0). The red dashed line shows deviation from Eq. (4.23) at large distances, while black dashed line illustrates transition to power law dependence, as in Eq. (4.25).

Table 4.1: Fitting parameters I_0, d_0, A α, B and β for few (n,0) tubes. I_0 and d_0 are fitted in the range $2\text{Å} \leq d \leq 20\text{Å}$ for $Z=3$; A and α are computed using $d=3\text{Å}$; while B and β are computed for $Z=3$ and fitted for $d \geq 22\text{Å}$.

tube	$d_t(nm)$	I_0 (eV)	d_0 (Å)	A (meV)	α	B (meV)	β
(8,0)	0.63	0.29	1.71	1.82	3.00	3.78	3.56
(10,0)	0.79	0.25	2.33	3.42	2.71	8.11	3.60
(11,0)	0.87	0.22	2.33	2.94	2.74	4.00	3.58
(13,0)	1.03	0.20	2.89	4.04	2.60	6.98	3.57
(14,0)	1.11	0.19	2.80	3.63	2.63	4.22	3.61
(16,0)	1.27	0.18	3.31	4.07	2.56	5.80	3.48

the center of mass. For large distances the binding energy scales as

$$I_E = B\left(\frac{d_t}{d}\right)^{\beta} \tag{4.25}$$

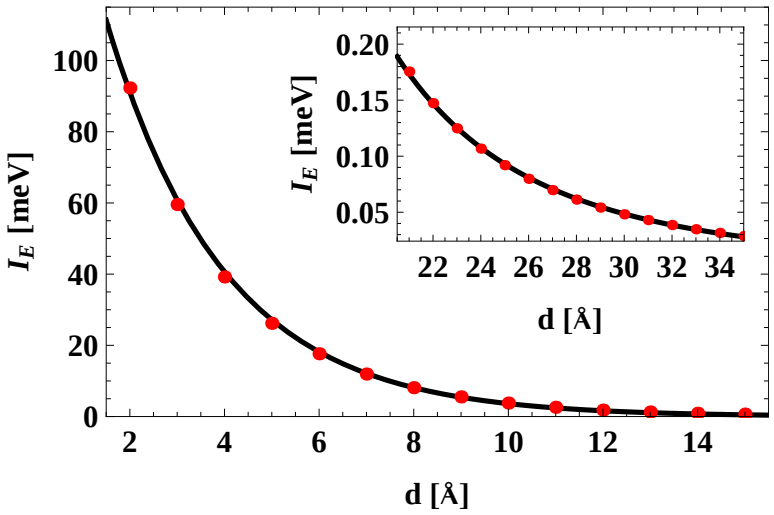

Figure 4.11: Best fit of I_E for small and large distances (inset) for an (11,0) tube. Solid curves correspond to Eqs.(4.23-4.25) while red points are calculated data points.

The fitting parameters B and β were computed for several SWNTs and the results are summarized in Table 4.1. We can carry out a similar scaling analysis for the dependence of I_E on Z, effective valency of the impurity ion at fixed ion position. We found the power law dependence

$$I_E(Z) = AZ^{\alpha} \tag{4.26}$$

The fitting constants A and α are summarized in Table 4.1 for zigzag SWNTs for $d = 3$Å. In Figs. 4.13-4.14, we show plots of the fitting parameters.

4.6 Summary

In summary, we have shown that a single charged impurity can induce exction localization in SWNT. The impurity binding energies can range from few meV to hundreds of meV depending on main parameters of the model: the diameter of tube, d_t, effective charge of impurity ion, Z, and the distance of the ion from the surface of the SWNT, d. The binding energy has weak dependence on the position of the ion

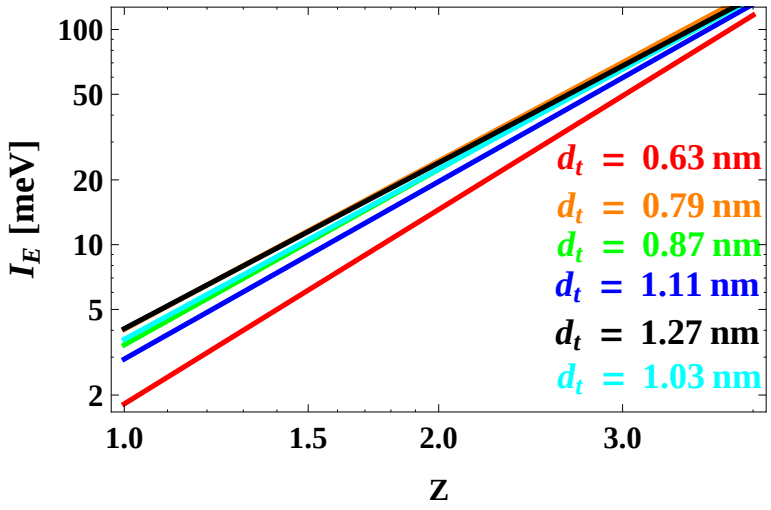

Figure 4.12: Impurity binding energy I_E (log-log scale) for different SWNTs plotted as a function of the effective charge Z of impurity ion for $d = 3$ Å: red curve is for an (8,0) SWNT, Green for (10,0) tube, blue for (11,0) tube, orange for (13,0) tube, cyan for (14,0) tube, and black for (16,0) tube

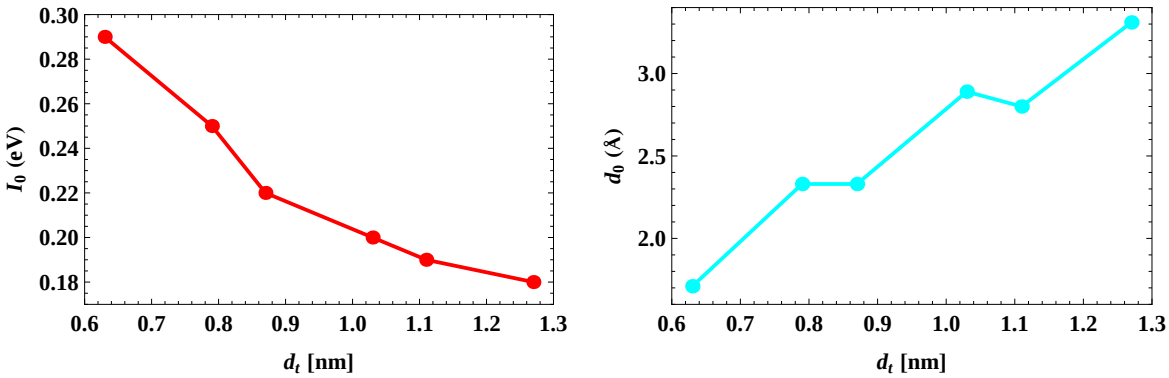

Figure 4.13: Fitting parameters vs tube diameter, d_t : (left panel) is for the parameter I_0; and (right panel) is for d_0.

on the SWNT surface for the fixed main parameters. We also obtained analytical fits for dependence on exciton binding on main model parameters.

In the next chapter, our model will be applied for the calculation of the optical

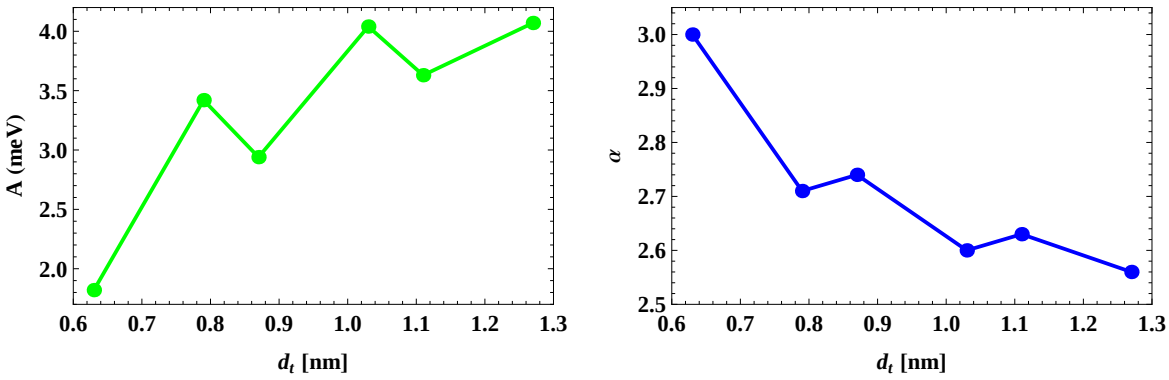

Figure 4.14: Fitting parameters vs tube diameter, d_t : (left panel) is for the parameter A; and (right panel) is for α.

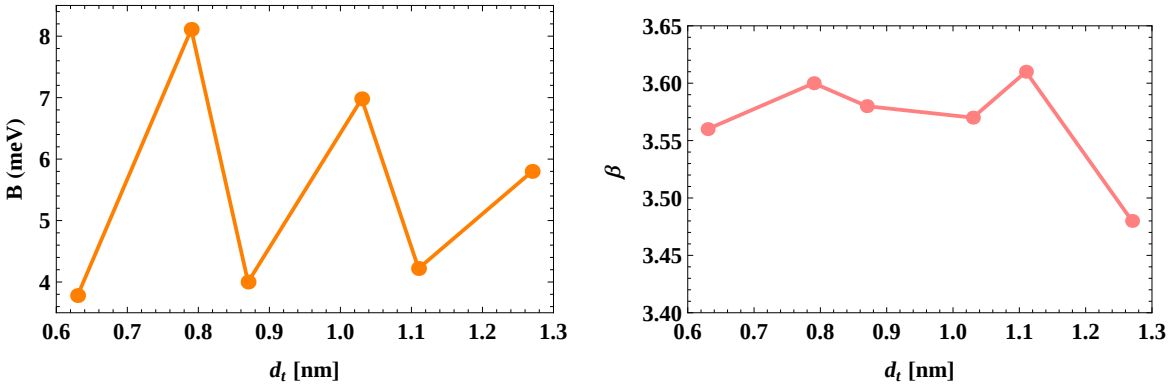

Figure 4.15: Fitting parameters vs tube diameter, d_t : (left panel) is for the parameter B; and (right panel) is for β.

properties of SWNTs with charged impurity atom absorbed on its surface. This calculation facilitates comparison of our theoretical predictions with the experiments.

Chapter 5

Optical spectra in the presence of impurity

In this chapter, we study the effect of a single charged impurity on the optical spectra in semiconducting SWNTs. The most important measurable quantity we address here is the absorption coefficient $\alpha(\omega)$ which gives the interaction of an external light field with excitations in the system.

The optical properties of solids provide an important tool for studying energy band structure, impurity levels, excitons, localized defects, lattice vibrations, and certain magnetic excitations. By measuring reflectivity, transmission, or absorption, one can deduce the complex dielectric function $\epsilon(\omega)$, the optical conductivity $\sigma(\omega)$, absorption coefficient $\alpha(\omega)$, or the fundamental excitation energies. The optical properties of solids are determined by interaction of an external light field with excitations in the system. In treating a solid therefore, we will need to consider contributions to the optical properties from various electronic transition processes. To begin with, there are *intraband processes* which correspond to the electronic conduction and are dominated by free carriers, and hence are more important in conducting materials such as metals, semimetals and degenerate semiconductors. These intraband processes can be understood in their simplest terms by the classical Drude theory, or in more detail by solving the Boltzmann equation. In addition to

the intraband (free carrier) processes, there are *interband processes* which correspond to the absorption of electromagnetic radiation by an electron in an occupied state below the Fermi level, thereby inducing a transition to an unoccupied state in a higher band. This interband process is intrinsically a quantum mechanical process and must be discussed in terms of quantum mechanical concepts. In a semiconductor at low frequencies, the principal electronic conduction mechanism is associated with free carriers. As the photon energy increases and becomes comparable to the energy gap, a new conduction process can occur. A photon can excite an electron from an occupied state in the valence band to an unoccupied state in the conduction band. In this process the photon is absorbed, an excited electronic state is formed and a hole is left behind.

Single-wall carbon nanotubes as prototypical one-dimensional structures have well defined optical properties. Hence, optical spectroscopy methods, such as absorption, photoluminescence, Rayleigh, and Raman scattering have become important characterization techniques for carbon nanotubes [87–89]. They allow the identification of the nanotube microscopic structure or chirality of isolated tubes as well as for samples containing millions of tubes.

We will obtain an expression for the absorption coefficient for the free-electron interband transitions and then from it, we derive that for excitons and later that for bound excitons.

5.1 The absorption coefficient for SWNT

In the presence of an optical field, a material responds by forming a microscopic dipole density resulting in a polarization $P(\mathbf{r}, t)$ of the material. In linear and homogeneous materials, the polarization and the optical field are parallel [91]

$$P(\omega) = 4\pi\chi(\omega)\mathcal{E}(\omega) \tag{5.1}$$

The proportionality coefficient is given by the optical susceptibility $\chi(\omega)$ describing the linear response of the system to a perturbation in a spatially homogeneous

system. The intensity $I(z)$ of an electromagnetic wave propagating in the z direction is given by [90, 91]

$$I(z) = \mathcal{E}^2 e^{-\alpha(\omega)z} \tag{5.2}$$

with the absorption coefficient

$$\alpha(\omega) = \frac{4\pi\omega}{\hbar n_b c}\mathrm{Im}\chi(\omega) \tag{5.3}$$

describing the propagation depth of light in the material. Here, $\mathcal{E}$ is the amplitude of the electric field of the photon, ω is the photon energy, c is the speed of light, n_b is the background refractive index, and $\hbar$ is the reduced Planck constant. The calculation of $\alpha(\omega)$ requires the knowledge of the optical susceptibility $\chi(\omega)$. For interband optical absorption, the optical susceptibility is given by [91]

$$\chi(\omega) = \sum_{cv\mathbf{k}} \frac{|\vec{\eta}\cdot\langle c\mathbf{k}|\vec{p}|v\mathbf{k}\rangle|^2}{V}\left[\frac{1}{\omega + E_{cv\mathbf{k}} + i\Gamma} - \frac{1}{\omega - E_{cv\mathbf{k}} + i\Gamma}\right] \tag{5.4}$$

where V is the integration volume, $\vec{\eta}$ the electric field polarization vector, $\vec{p}$ is the dipole operator, and $E_{cv\mathbf{k}} = E_{c\mathbf{k}} - E_{v\mathbf{k}}$ is the energy difference between the initial and the final state. According to Eq. (5.3), the absorption spectrum for interband processes (α^{ib}) is determined by the imaginary part of $\chi(\omega)$

$$\begin{aligned}\alpha^{ib}(\omega) &= \frac{4\pi\omega}{\hbar n_b c}\mathrm{Im}\chi(\omega) \\ &= \frac{4\pi^2\omega}{\hbar n_b c V}\sum_{cv\mathbf{k}} |\vec{\eta}\cdot\langle c\mathbf{k}|\vec{p}|v\mathbf{k}\rangle|^2\delta(\omega - E_{cv\mathbf{k}})\end{aligned} \tag{5.5}$$

The delta function $\delta(x)$ can be replaced with a Lorentzian function as

$$\delta(x) = \frac{1}{\pi}\lim_{\Gamma\to 0}\frac{\Gamma}{x^2 + \Gamma^2} \tag{5.6}$$

where Γ is spectral broadening.

In SWNTs, it was thought for a long time that optical excitations were completely understood within the one-particle picture [87]. In this picture, the interband transitions are governed by van Hove singularities in the density of states

and absorption spectra due to quasi-1D nature of SWNTs electrons [1, 92]. Optical properties based on initial free-electron band-to-band transitions provide useful insights on chirality-dependent studies of SWNTs. In contrast, theoretical calculations predicted the excitonic character of optical excitations in semiconducting nanotubes [25]. This makes sense because the strong spatial confinement of carriers in one-dimensional materials due to enhanced electron-hole Coulomb interaction leads to the formation of strongly bound excitons. Excitonic effects should therefore dominate the optical transitions in semiconducting SWNTs because the exciton binding energy ($\approx 0.2 - 1$ eV, depending on tube diameter, chirality, and dielectric screening [67]) is much larger than the thermal energy at room temperature [29]. The formation of strongly bound excitons in SWNTs affects both the transitions energies and the shape of the optical spectra [16]. From an experimental point of view, two-photon absorption experiments have also confirmed the crucial role of excitons in the optical properties of semiconducting carbon nanotubes [29]. Recently, theoretical studies on the optical properties of metallic SWNTs [93, 94] reveal surprisingly that excitonic effects significantly change the properties of metallic SWNTs as well. However, the excitonic binding energies in metallic nanotubes is around one order of magnitude smaller than in semiconducting tubes of comparable diameter. In what follows, we discuss the contribution to the optical properties of semiconducting SWNTs by excitonic effects.

In the excitonic picture, the absorption coefficient $\alpha^0(\omega)$ can be expressed as [68]

$$\alpha^0(\omega) = \frac{4\pi^2\omega}{\hbar n_b c V} \sum_{nQ} |M_{nQ}|^2 \delta\big(\omega - \Omega_B^{(n)}(Q)\big) \tag{5.7}$$

where M_{nQ} is the optical matrix element and $\Omega_B^{(n)}(Q)$ the excitation energy for bright excitons. The matrix element M_{nQ} is given by

$$\begin{aligned} M_{nQ} &= \langle GS|\vec{p}\cdot\vec{\eta}|nBQ\rangle \\ &= \sum_k A_{B,Q}^{(n)}(k)\langle\psi_{c\mu k+Q}|\vec{p}\cdot\vec{\eta}|\psi_{v\mu k}\rangle \end{aligned} \tag{5.8}$$

where $|GS\rangle$ is the ground state of the SWNT crystal, $\vec{p}$ is the dipole operator, $\vec{\eta}$ is the polarization vector of light, and ψ is the single-particle wave function of the

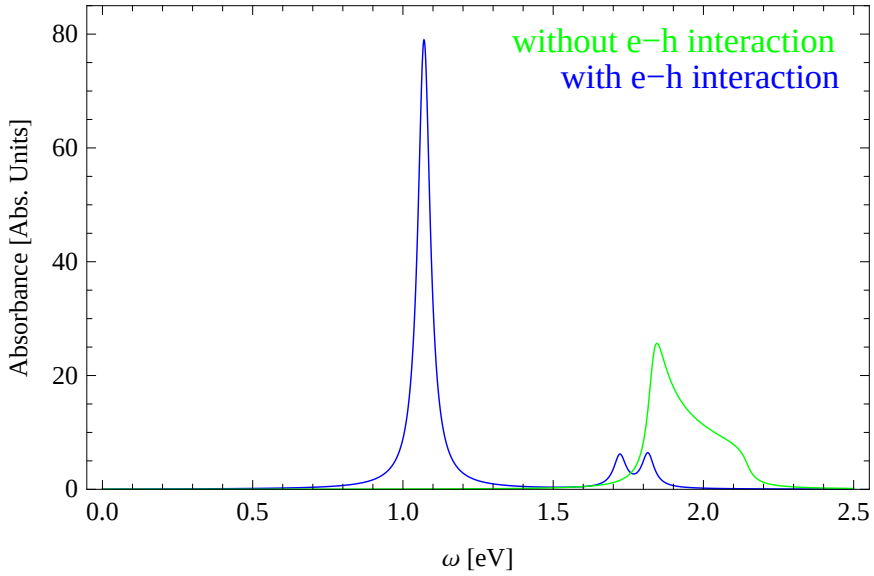

Figure 5.1: Illustrated absorption spectra (not to scale) for an (11,0) SWNT plotted against photon energy ω: (green) is for the interband absoprtion $\alpha^{ib}(\omega)$; and (blue) is for the excitonic absorption $\alpha^{0}(\omega)$. Coulomb effects lead to the formation of strongly bound excitons due the electron-hole interactions. The optical spectra is reshaped from a van Hove singularity into a Lorentzian. Both spectra are computed with a broadening of $\Gamma = 25$ meV.

electron. The calculation of the optical matrix element M_{nQ} is crucial in determining the optical properties. Without the electron-hole interaction, the excitations are given by vertical transitions between independent hole and electron states, and Eq. (5.7) reduces to the interband expression in Eq. (5.5). As an illustration, we show in Fig. 5.1 the absorbtion spectra for an (11,0) in both the free-particle and excitonic pictures.

5.2 Absorption coefficient in the presence of impurity

In order to facilitate comparison of our theoretical predictions with the experiments, we calculate the absorption coefficient $\alpha(\omega)$ of the system. Within our model we

need to include only the states originated from the bright exciton manifold with the wave function of ith eigenstate:

$$\Psi^{(i)}(\mathbf{r}_e, \mathbf{r}_h) = \sum_{nQ} \mathcal{C}^{(i)}_{BnQ} \Phi^{(n)}_{B,Q}(\mathbf{r}_e, \mathbf{r}_h) \tag{5.9}$$

Interaction of the excitons with the light of polarization $\vec{\eta}$, is given by the absorption coefficient (per atom): [91, 95]

$$\alpha(\omega) = \frac{4\pi^2\omega}{\hbar n_b c} \sum_i |M^{(i)}|^2 \delta(\omega - E^{(i)}) \tag{5.10}$$

where ω is the energy of incident photon, c is the speed of light, n_b is the background refractive index ($n_b = 1$ for suspended tubes), $\hbar$ the reduced Planck constant, and the matrix element is as follows:

$$\begin{aligned} M^{(i)} &= \langle GS|\vec{p}\cdot\vec{\eta}|\Psi^{(i)}\rangle \\ &= \sum_{nQ} \mathcal{C}^{(i)}_{BnQ} M_{nQ} \end{aligned} \tag{5.11}$$

where M_{nQ} is the optical matrix element given in Eq. (5.8). In the absence of the impurity, the excitations of the system are solutions of the bare BS equation and Eq. (5.10) reduces to: [68]

$$\alpha^{(0)}(\omega) = \frac{4\pi^2\omega}{\hbar n_b c} \sum_{nQ} |M_{nQ}|^2 \delta\big(\omega - \Omega^{(n)}_B(Q)\big) \tag{5.12}$$

It is very instructive to visualize all scattered excitonic states by plotting the density of states (DOS) because some of those energy levels may have negligible dipole matrix elements. The DOS is given by:

$$\rho(\omega) = \sum_i \frac{\Gamma}{(\omega - E^{(i)})^2 + \Gamma^2} \tag{5.13}$$

where we replace the Dirac delta function with a Lorentzian with the line width Γ. The DOS for the (11,0) SWNT is shown in Fig. 5.2 for different values of 5meV $\leq \Gamma \leq$ 28meV. Two bound levels are clearly seen at $E^{(1)} = 1.054$ eV and

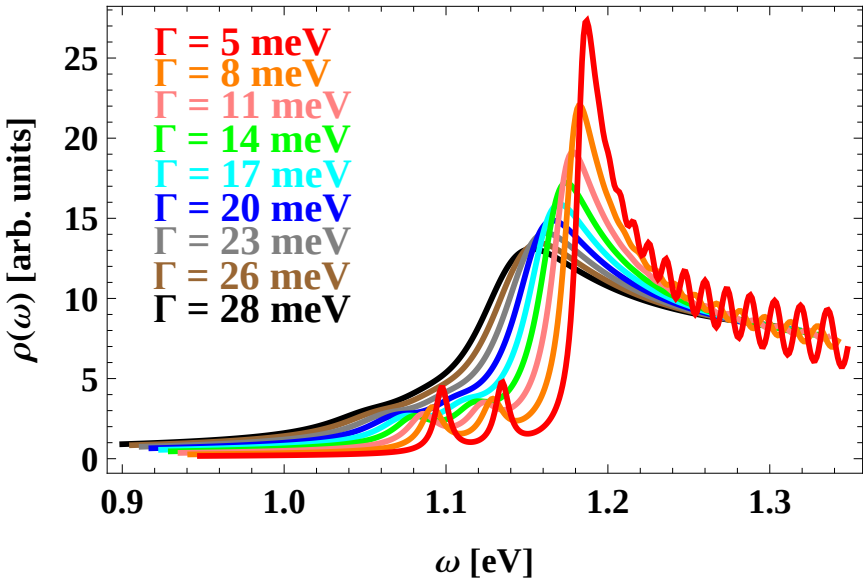

Figure 5.2: Density of states (offset for clarity) of (11,0) SWNT computed for $Z = 3$ and $d = 2$ Å, $\rho(\omega)$, plotted for different values of the spectral broadening Γ, shown in the legend.

$E^{(2)} = 1.089$ eV, both corresponding to the impurity induced localized states, as we prove next.

The absorption of light with $\vec{\eta_z}$ (axial) polarization for the (11,0) SWNT is shown in Fig. 5.3. Since the total oscillator strength of non-localized excitonic states is larger than the one of the bound state from a single impurity, we compute the differential absorption coefficient, that is, the difference in absorption in the presence of the impurity and in the free exciton picture:

$$\Delta\alpha(\omega) = \alpha(\omega) - \alpha^{(0)}(\omega). \tag{5.14}$$

Using the line broadening of 10 meV we plot in Fig. 5.3 the spectrum of the differential absorption along with the bare absorption spectrum for (11,0) nanotube. The same two peaks show up in the differential absorption, red shifted from the bare lowest bright exciton position $\Omega_B^{(1)}(0) = 1.135$ eV, due to the perturbation of the impurity. Since these two peaks are below the onset of bright exciton continuum they can be are attributed to impurity induced localized states with the binding energies

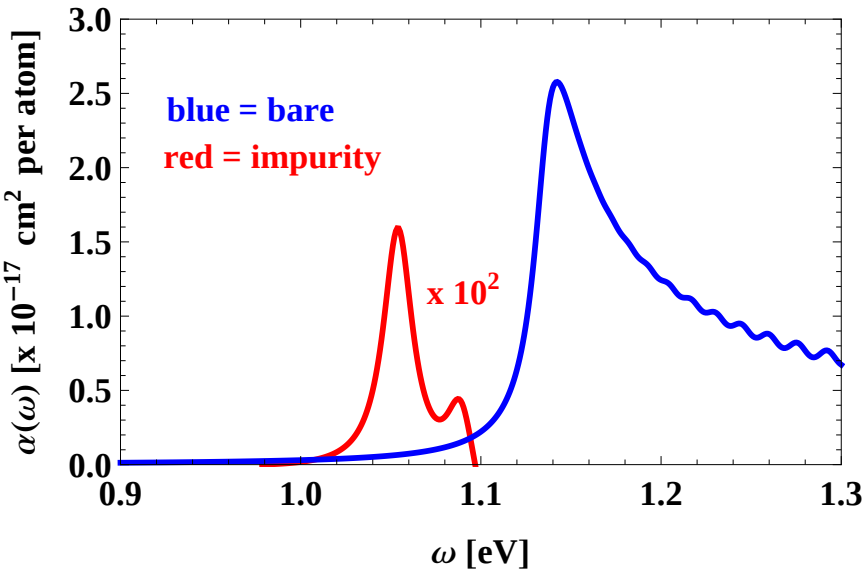

Figure 5.3: Absorption coefficient, computed with 10 meV broadening: (blue) absorption coefficient for the bare SWNT, $\alpha^{(0)}(\omega)$; (red) differential absorbance in the presence of the impurity, $\Delta\alpha(\omega)$ (scaled by a factor of 100).

$E_b = 81$ meV and 46 meV respectively. Additional proof of their localization can be presented by visualizing the wave function, or the local optical DOS, which we discuss next.

We introduce the partial absorption coefficient $\alpha(z,\omega)$. In calculating $\alpha(z,\omega)$ we use the dipole matrix element, integrated out only within a narrow belt, containing one ring of carbon atoms:

$$\alpha(j,\omega) = \frac{4\pi^2\omega}{\hbar n_b c}\sum_i |M^{(i)}(j)|^2\delta(\omega - E^{(i)}) \tag{5.15}$$

here j labels the ring position within the finite size SWNT, $-L/2T \le j \le L/2T$. Corresponding matrix element is given by:

$$\begin{aligned} M^{(i)}(j) &= -e\sum_{nQ}\sum_{sk} \mathcal{C}^{(i)}_{BnQ} e^{iQ(z_s+jT)} A^{(n)}_{B,Q}(k) \times \\ &\quad \times C^{c}_{\mu k+Q}(s)(z_s+jT)C^{v*}_{\mu k}(s) \end{aligned} \tag{5.16}$$

In the absence of impurity one has to replace $E^{(i)}$ in Eq. (5.15) with the bare exciton energy $\Omega^{(n)}_B(Q)$, the index of summation $i \to n,Q$ and use bare dipole matrix element

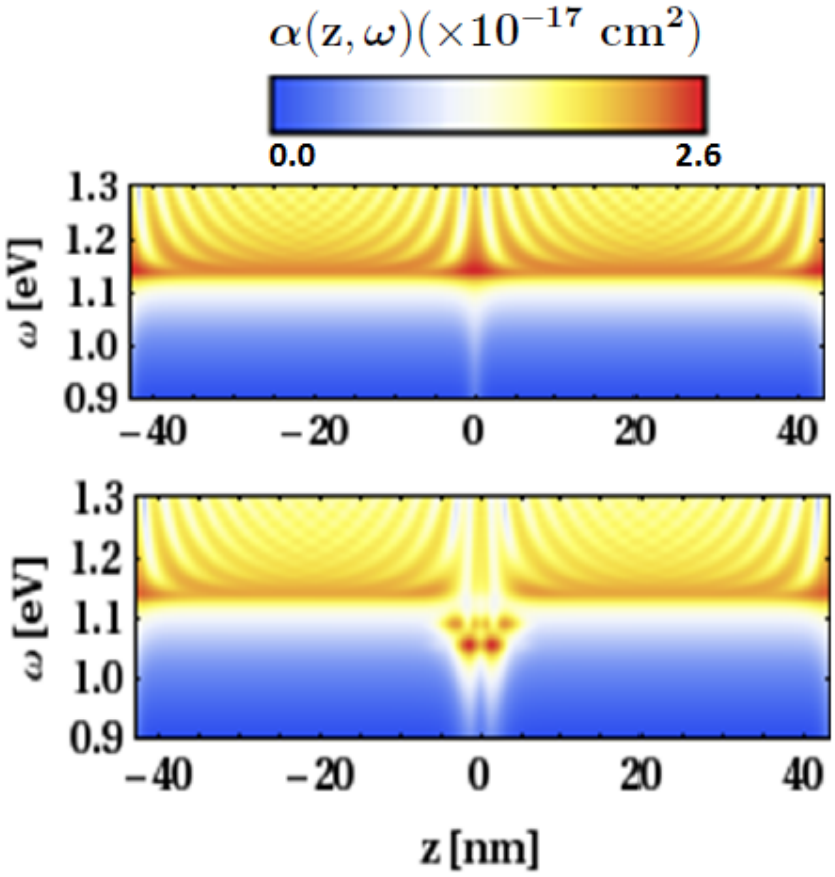

Figure 5.4: Map of the partial absorption coefficient (per atom) vs. photon energy, ω, and axial position, z, along the SWNT for the $\vec{\eta_z}$ polarization of light for (11,0) nanotube, $d = 2$ Å and $Z = 3$. (top) for bare SWNT; (bottom) in the presence of impurity at $z = 0$.

given by:

$$M_{nQ}(j) = -e \sum_{sk} e^{iQ(z_s+jT)} A^{(n)}_{B,Q}(k) \times \\ \times C^{c}_{\mu k+Q}(s)(z_s + jT) C^{v*}_{\mu k}(s) \tag{5.17}$$

The partial absorption coefficient map, shown in Fig. 5.4 as a function of the photon energy and axial position along the SWNT, has the same low energy spectral features, as seen in Fig. 5.3. However, the bound states have very low optical density far away from the impurity position at $z = 0$, with the characteristic localization

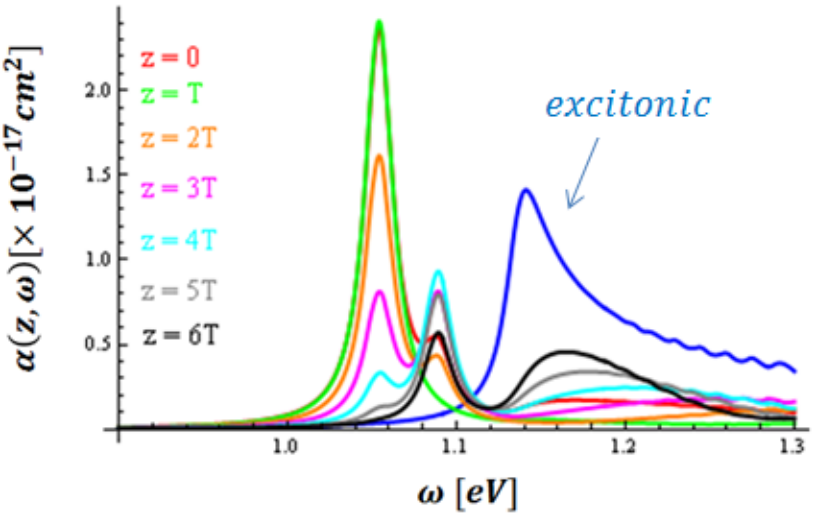

Figure 5.5: Absorption cross section for different axial position, z, along the SWNT with the impurity ion at $z = 0$. The blue curve corresponds to the bare excitonic absorption coefficient.

length of several nm. This is why the partial absorption is almost the same as in the bare SWNT outside the central region, near the ion. In Fig. 5.5, we show the absorption cross section for different axial position z along the SWNT. It shows that the absorption is local and dies out as the distance from impurity is increased.

5.3 Further results

We present additional results for the density of states and absorption coefficient for few $(n, 0)$ tubes, we also show dependence of density of states for different effective valency charge (Z) of the impurity ion, and finally the local absorption distribution profile for two additional tubes. All spectra have been computed for $d = 2$Å and with a broadening of $\Gamma = 10$ meV.

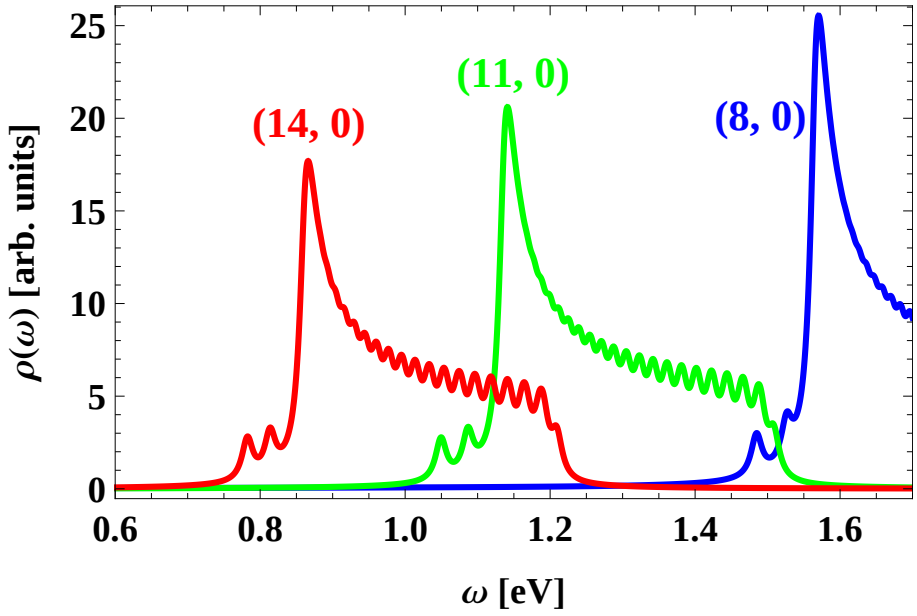

(a)

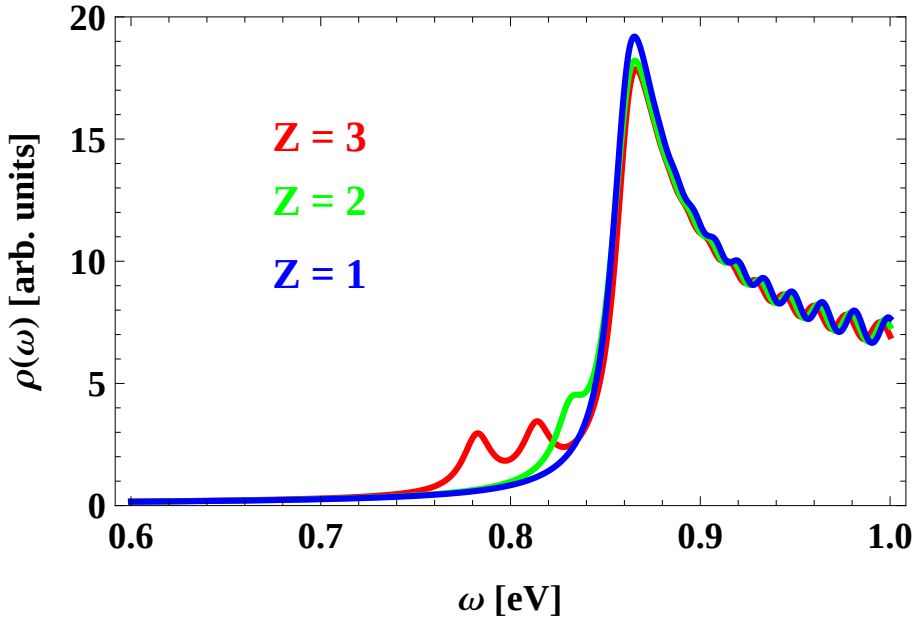

(b)

Figure 5.6: (a) Density of states for different (n,0) SWNTs computed for $Z = 3$ and $d = 2$ Å, $\rho(\omega)$, plotted with a spectral broadening $\Gamma = 10$ meV: (blue) for (8,0) tube; (green) for (11,0) tube; and (red) for (14,0) tube. (b) Density of states for (14,0) SWNT for different Z, computed for $d = 2$ Å: (blue) is for $Z = 1$; (green) for $Z = 2$, and (red) for $Z = 3$.

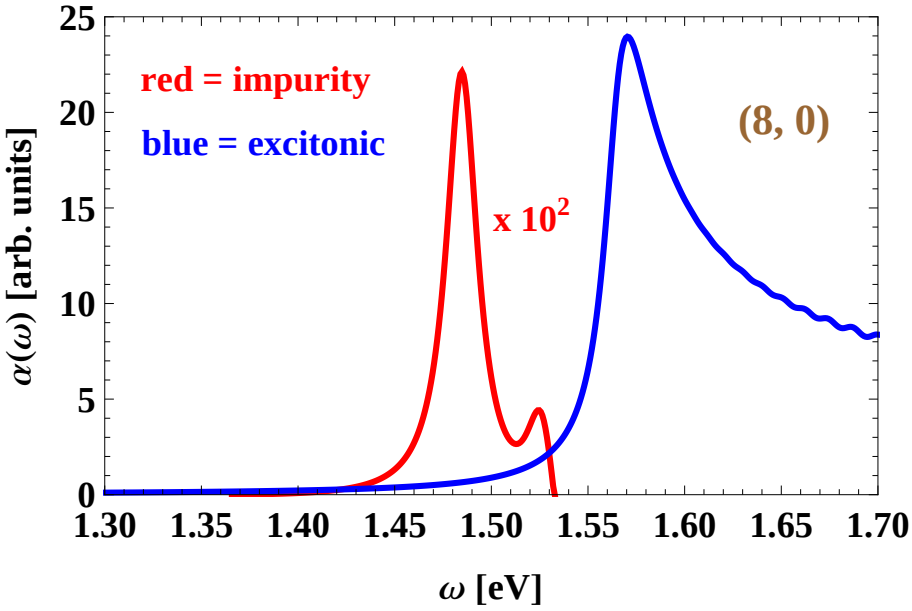

(a)

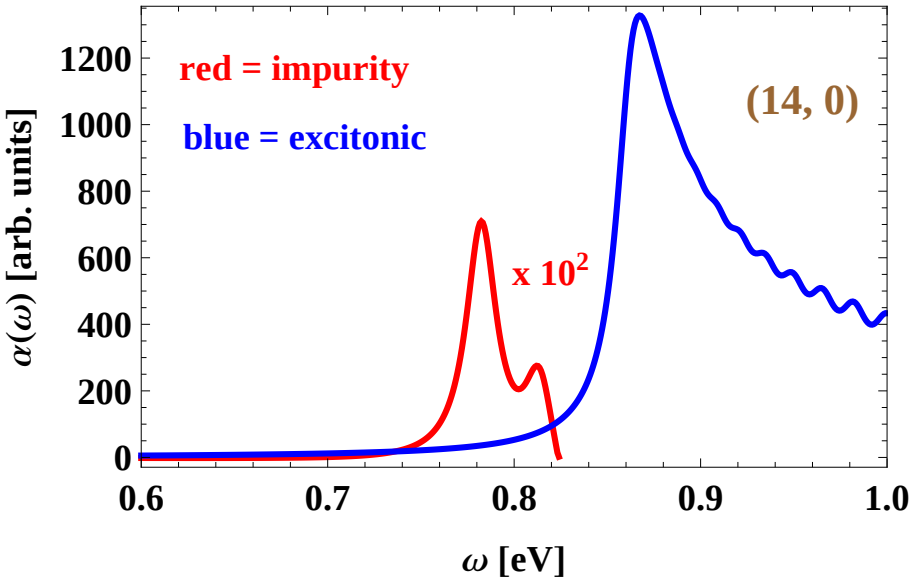

(b)

Figure 5.7: Absorption coefficient, computed with 10 meV broadening: (blue) absorption coefficient for the bare SWNT, $\alpha^{(0)}(\omega)$; (red) differential absorbance in the presence of the impurity, $\Delta\alpha(\omega)$ (scaled by a factor of 100): (a) for (8,0) tube; (b) for (14,0) tube.

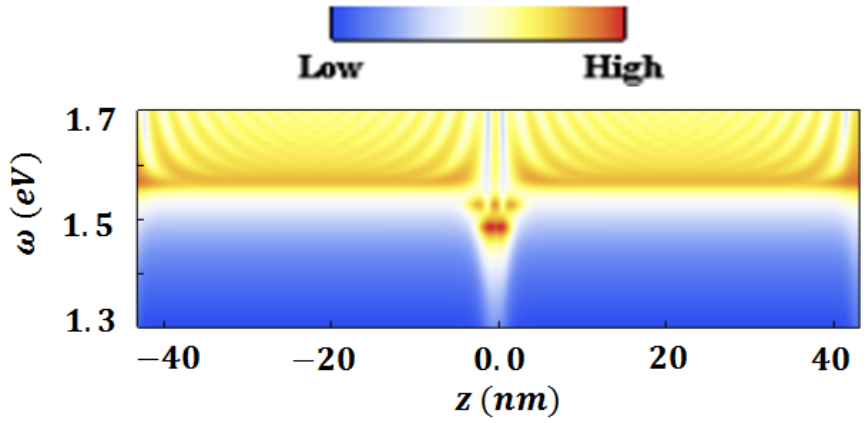

(a)

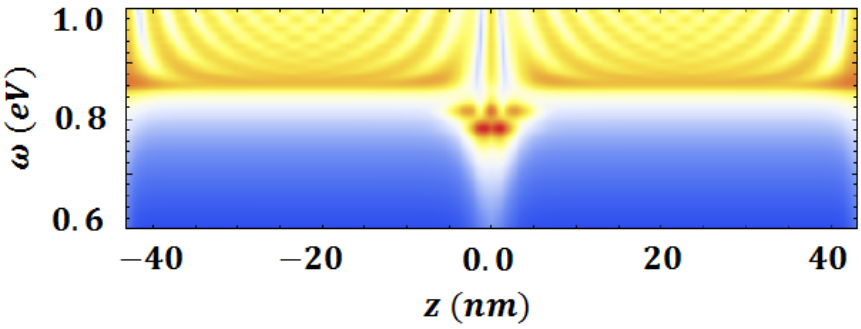

(b)

Figure 5.8: Map of the partial absorption coefficient vs. photon energy, ω, and axial position, z, along the SWNT for the $\vec{\eta_z}$ polarization of light for $d = 2$Å and $Z = 3$, with the impurity at $z = 0$: (a) for (8,0) tube; (b) for (14,0) tube.

Chapter 6

Conclusions and perspectives

In summary, we have shown that a single charged impurity can induce exciton localization in SWNT. The states localized by the impurity can have binding energies ranging from few meV to hundreds of meV depending on the geometry of the actual SWNT-ion complex. We calculated this dependence and parameterized it for three main parameters of the model: the SWNT diameter, d_t, the effective charge of the impurity ion, Z, and the distance of the ion from the surface of the SWNT, d. The binding energy has a weak dependence on the position of the ion on the SWNT surface for the fixed main parameters. Thus one may expect that in certain cases the impurity could be mobile on the tube surface. Localization length of the impurity bound exciton also varies, being as small as several nanometers for $Z = 3$, tri-valent ion at the distance $d = 2$ Å from the SWNT surface.

The absorption of molecules to the surface of carbon nanostructures opens a new field of hybrid systems with distinct and controllable properties. We present a microscopic study of the optical absorption in carbon nanotubes functionalized with an immobile charge impurity. As a result, the absorption spectra of functionalized tubes reveal a considerable redshift of transition energies depending on the effective valency of the immobile charge and distance from the SWNT surface.

SWNTs consist of a single layer of carbon atoms show a high sensitivity to changes in their surrounding medium, making them good candidates for sensitive

nanoscale detectors The functionalization of nanotubes enables the control and optimization of their properties and is a promising strategy to exploit their tremendous application potential.

Bibliography

[1] R. Saito, G. Dresselhaus, and M. S. Dresselhaus, *Physical Properties of Carbon Nanotubes*, (Imperial College Press, 1998).

[2] S. Reich, C. Thomsen, and J. Maultzsch, *Carbon Nanotubes: Basic Concepts and Physical Properties* (Wiley-VCH, Berlin, 2004).

[3] S. Iijima, "Helical microtubules of graphitic carbon," Nature **354**, 56 (1991).

[4] D.S. Bethune, C.H. Klang, M.S. de Vries, G. Gorman, R. Savoy, J. Vazquez, and R. Beyers, "Cobalt catalysed growth of carbon nanotubes with single-atomic-layer walls," Nature **363**, 605 (1993).

[5] S. Iijima and T. Ichihashi, "Single-shell carbon nanotubes of 1-nm diameter," Nature **363**, 603 (1993).

[6] K. S. Novoselov, A. K. Geim, S. V. Morozov, D. Jiang, Y. Zhang, S. V. Dubonos, I. V. Grigorieva, and A. A. Firsov, "Electric field effect in atomically thin carbon films," Science **306**(5696), 666 (2004).

[7] K. S. Novoselov, D. Jiang, F. Schedin, T. J. Booth, V. V. Khotkevich, S. V. Morozov, and A. K. Geim, "Two-dimensional atomic crystals," Proc. Natl. Acad. Sci. USA **102**(30), 10451 (2005).

[8] P. L. McEuen, M. S. Fuhrer, and H. Park, "Single-walled carbon nanotube electronics," IEEE Transactions on Nanotechnology **1**(1), 78 (2002).

[9] M. J. O'Connell, S. M. Bachilo, C. B. Huffman, V. C. Moore, M. S. Strano, E. H. Haroz, K. L. Rialon, P. J. Boul, W. H. Noon, C. Kittrell, J. Ma, R. H. Hauge, R. B. Weisman and R. E. Smalley, "Band gap fluorescence from individual single walled carbon nanotubes," Science **297**, 297 (2002).

[10] M. S. Dresselhaus, G. Dresselhaus, R. Saito, A. Jorio, "Raman spectroscopy of carbon nanotubes," Phys. Rep. **409**, 47 (2005).

[11] C. Fantini, A. Jorio, M. Souza, M. S. Strano, M. S. Dresselhaus, and M. A. Pimenta, "Optical transition energies for carbon nanotubes from resonant Raman spectroscopy: environment and temperature effects," Phys. Rev. Lett. **93**, 147406 (2004).

[12] A. Jorio, C. Fantini, M. A. Pimenta, R. B. Capaz, Ge. G. Samsonidze, G. Dresselhaus, and M. S. Dresselhaus, "Resonance Raman spectroscopy (n, m)-dependent effects in small-diameter single-wall carbon nanotubes," Phys. Rev. B **71**, 075401 (2005).

[13] Ge. G. Samsonidze, R. Saito, N. Kobayashi, A. Grüneis, J. Jiang, A. Jorio, S. G. Chou, G. Dresselhaus, and M. S. Dresselhaus, "Family behavior of the optical transition energies in single-wall carbon nanotubes of smaller diameters," Appl. Phys. Lett. **85**, 5703 (2004).

[14] J. U. Lee, "Band-gap renormalization in carbon nanotubes: Origin of the ideal diode behavior in carbon nanotube p-n structures'" Phys. Rev. B **75**, 075409 (2007).

[15] G. Dukovic, F. Wang, D. Song, M. Sfeir, T. Heinz, and L. Brus, "Structural Dependence of Excitonic Optical Transitions and Band-Gap Energies in Carbon Nanotubes," Nano Lett. **5**, 2314, (2005).

[16] E. Malić, M. Hirtschulz, F. Milde, M. Richter, J. Maultzsch, S. Reich, and A. Knorr, "Coulomb effects in single-walled carbon nanotubes," Phys. Stat. Sol. B **245**, 2155 (2004).

[17] T. Ando, "Excitons in carbon nanotubes," J. Phys. Soc. Jpn. **66**, 1066 (1997).

[18] S. V. Rotkin, and S. Subramoney (eds.), *Applied Physics Of Carbon Nanotubes: Fundamentals Of Theory, Optics And Transport Devices* (Springer-Verlag, Berlin, 2005).

[19] A, Jorio, M. S. Dresselhaus and G. Dresselhaus *Carbon Nanotubes: Advanced Topics in the Synthesis, Structure, Properties and Application*, (Springer, New York, 2008).

[20] F. Xia, M. Steiner, Y. -M. Line, and Ph. Avouris, "A microcavity-controlled, current-driven, on-chip nanotube emitter at infrared wavelengths," Nature Nanotechnol. **3** , 609 (2008).

[21] P. Avouris, M. Freitag and V. Perebeinos, "Carbon-nanotube photonics and optoelectronics," Nature Photon. **2**, 341 (2008).

[22] J. -H. Han, G. L. C. Paulus, R. Maruyama, D. A. Heller, W. -J. Kim, P. W. Barone, C. Y. Lee, J. H. Choi, M. -H. Ham, C. Song, C. Fantini, and M. S. Strano, "Exciton antennas and concentrators from coreshell and corrugated carbon nanotube filaments of homogeneous composition," Nature Mater. **9**, 833 (2010).

[23] T. Hertel, "Carbon nanotubes: A brighter future," Nature Photonics **4**, 77 (2010).

[24] T.G. Pedersen, "Variational approach to excitons in carbon nanotubes," Phys. Rev. B **67**, 073401 (2003).

[25] C.D. Spataru, S. Ismail-Beigi, L.X. Benedict, and S.G. Louie, "Excitonic effects and optical spectra of single-walled carbon nanotubes," Phys. Rev. Lett. **92**, 077402 (2004).

[26] C.D. Spataru, S. Ismail-Beigi, L. X. Benedict, and S.G. Louie, "Quasiparticle energies, excitonic effects and optical spectra of small diameter single-walled carbon nanotubes," Appl. Phys. A **78**, 1129 (2004).

[27] C.D. Spataru, S. Ismail-Beigi, R. B. Benedict, and S.G. Louie, "Theory and ab initio calculation of radiative lifetime of excitons in semiconducting carbon nanotubes," Phys. Rev. Lett. **95**, 247402 (2005).

[28] E. Chang, G. Bussi, A. Ruini, and E. Molinari, "Excitons in carbon nanotubes: an ab initio symmetry-based approach," Phys. Rev. Lett. **92**, 113410 (2004).

[29] F. Wang, G. Dukovic, L.E. Brus, and T.F. Heinz, "The optical resonances in carbon nanotubes arise from excitons," Science **308**, 838 (2005).

[30] J. Maultzsch, R. Pomraenke, S. Reich, E. Chang, D. Prezzi, A. Ruini, E. Molinari, M.S. Strano, C. Thonsen, and C. Lienau, "Exciton binding energies in carbon nanotubes from two-photon photoluminescence," Phys. Rev. B **72**,241402(R) (2005).

[31] J. Lefebvre, D. G. Austing, J. Bond and P. Finnie, "Photoluminescence imaging of suspended single-walled carbon nanotubes," Nano Lett. **6**, 1603 (2006).

[32] J. Shaver, J. Kono, O. Portugall, V. Krstić, G. L. J. A. Rikken, Y. Miyauchi, S. Maruyuma, and V. Perebeinos, "Magnetic Brightening of Carbon Nanotube Photoluminescence through Symmetry Breaking," Nano Lett. **7**, 1851 (2007).

[33] I. B. Mortimer and R. J. Nicholas, "Role of Bright and Dark Excitons in the Temperature-Dependent Photoluminescence of Carbon Nanotubes," Phys. Rev. Lett. **98**, 027404 (2007).

[34] R. Matsunaga, K. Matsuda, and Y. Kanemitsu, "Evidence for Dark Excitons in a Single Carbon Nanotube due to the Aharonov-Bohm Effect," Phys. Rev. Lett. **101**, 147404 (2008).

[35] D. M. Harrah, J. R. Schneck, A. A. Green, M. C. Hersam, L. D. Ziegler, and A. K. Swan, "Intensity-dependent exciton dynamics of (6,5) single-walled carbon nanotubes: momentum selection rules, diffusion, and nonlinear interactions," ACS Nano **5**, 9898 (2011).

[36] V. Perebeinos, J. Tersoff, and P. Avouris,"Effect of exciton-phonon coupling in the calculated optical absorption of carbon nanotubes," Phys. Rev. Lett. **94**, 027402 (2005).

[37] F. Plentz, H.B. Ribeiro, A. Jorio, M.S. Strano, and M.A. Pimenta, "Direct Experimental Evidence of Exciton-Phonon Bound States in Carbon Nanotubes," Phys. Rev. Lett. **95**, 247401 (2005).

[38] I.V. Bondarev, L.M. Woods, and K. Tatur,"Strong exciton-plasmon coupling in semiconducting carbon nanotubes," Phys. Rev. B **80**, 085407 (2009).

[39] V. Perebeinos, and P. Avouris, "Exciton Ionization, Franz-Keldysh, and Stark Effects in Carbon Nanotubes," Nano Lett. **7**, 609 (2007).

[40] A. Srivastava, H. Htoon, V.I. Klimov, and J. Kono, "Direct Observation of Dark Excitons in Individual Carbon Nanotubes: Inhomogeneity in the Exchange Splitting," Phys. Rev. Lett. **101**, 087402 (2008).

[41] K. Matsuda, Y. Miyauchi, T. Sakashita, and Y. Kanemitsu, "Nonradiative exciton decay dynamics in hole-doped single-walled carbon nanotubes," Phys. Rev. B **81**, 033409 (2010).

[42] R. Matsunaga, K. Matsuda, and Y. Kanemitsu, "Observation of Charged Excitons in Hole-Doped Carbon Nanotubes Using Photoluminescence and Absorption Spectroscopy," Phys. Rev. Lett. **106**, 037404 (2011).

[43] S. M. Santos, B. Yuma, S. Berciaud, J. Shaver, M. Gallart, P. Gilliot, L. Cognet, and B. Lounis, "All-Optical Trion Generation in Single-Walled Carbon Nanotubes," Phys. Rev. Lett. **107**, 187401 (2011).

[44] J. J. Crochet, J. G. Duque, J. H. Werner, and S. K. Doorn, "Photoluminescence imaging of electronic-impurity-induced exciton quenching in single-walled carbon nanotubes," Nature Nanotech. **7**, 126 (2012).

[45] Y. Ohno, S. Iwasaki, Y. Murakami, S. Kishimoto, S. Maruyama, and T. Mizutani, "Chirality-dependent environmental effects in photoluminescence of single-walled carbon nanotubes," Phys. Rev. B **73**, 235427 (2006).

[46] G. Dukovic, B. E. White, Z. Zhou, F. Wang, S. Jockusch, M. L. Steigerwald, T. F. Heinz, R. A. Friesner, N. J. Turro, and L. E. Brus, "Reversible Surface Oxidation and Efficient Luminescence Quenching in Semiconductor Single-Wall Carbon Nanotubes," J. Am. Chem. Soc. **126**, 15269 (2004).

[47] G. N. Ostojic, S. Zaric, J. Kono, M. S. Strano, V. C. Moore, R. H. Hauge, and R. E. Smalley, "Interband Recombination Dynamics in Resonantly Excited Single-Walled Carbon Nanotubes," Phys. Rev. Lett. **92**, 117402 (2004).

[48] M. Steiner, M. Freitag, V. Perebeinos, A. Naumov, J. P. Small, A. A. Bol, and P. Avouris, "Gate-Variable Light Absorption and Emission in a Semiconducting Carbon Nanotube," Nano Lett. **9**, 3477 (2009).

[49] E. Malic, C. Weber, M. Richter, V. Atalla, T. Klamroth, P. Saalfrank, S. Reich, and A. Knorr, "Microscopic Model of the Optical Absorption of Carbon Nanotubes Functionalized with Molecular Spiropyran Photoswitches," Phys. Rev. Lett. **106**, 097401 (2011).

[50] S. Ghosh, S. M. Bachilo, R. A. Simonette, K. M. Beckingham, and R. B. Weisman, "Oxygen Doping Modifies Near-Infrared Band Gaps in Fluorescent Single-Walled Carbon Nanotubes," Science **330**, 1656 (2010).

[51] T. Ignatova, H. Najafov, A. Ryasnyanskiy, I. Biaggio, M. Zheng, and S. V. Rotkin, "Significant FRET between SWNT/DNA and Rare Earth Ions: A Signature of Their Spatial Correlations," ACS Nano **5** (7), 6052, (2011).

[52] S. Manohar, T. Tang, and A. Jagota, "Structure of Homopolymer DNA-CNT Hybrids," J. Phys. Chem. C **111**, 17835 (2007).

[53] R. R. Johnson, A. T. Charlie Johnson, and M. L. Klein, "Probing the Structure of DNA-Carbon Nanotube Hybrids with Molecular Dynamics," Nano Lett. **8**, 69 (2008).

[54] S. V. Rotkin, "Electronic Properties of Nonideal Nanotube Materials: Helical Symmetry Breaking in DNA Hybrids," Annu. Rev. Phys. Chem. **61**, 241 (2010).

[55] H. Qian, P. T. Araujo, C. Georgi, T. Gokus, N. Hartmann, A. A. Green, A. Jorio, M. C. Hersam, L. Novotny, and Achim Hartschuh, "Visualizing the Local Optical Response of Semiconducting Carbon Nanotubes to DNA-Wrapping," Nano Lett. **8**, 2706 (2008).

[56] S. -Y. Ju, , J. Doll, I. Sharma, and F. Papadimitrakopoulos, "Selection of carbon nanotubes with specific chiralities using helical assemblies of flavin mononucleotide," Nature Nanotech. **3**, 356 (2008).

[57] R. Haggenmueller, S. S. Rahatekar, J. A. Fagan, J. Chun, M. L. Becker, R. R. Naik, T. Krauss, L. Carlson, J. F. Kadla, P. C. Trulove, D. F. Fox, H. C. DeLong, Z. Fang, S. O. Kelley, and J. W. Gilman, "Comparison of the quality of aqueous dispersions of single wall carbon nanotubes using surfactants and biomolecules," Langmuir, **24**, 5070 (2008).

[58] J. H. Choi and M. S. Strano, "Visualizing the Local Optical Response of Semiconducting Carbon Nanotubes to DNA-Wrapping," Appl. Phys. Lett. **90**, 223114 (2007).

[59] J. Lefebvre, J.M. Fraser, Y. Homma, and P. Finnie, "Photoluminescence from single-walled carbon nanotubes: a comparison between suspended and micelle-encapsulated nanotubes," Appl. Phys. A: Mater. Sci. Process. **78**, 1107 (2004).

[60] C. A. Silvera-Batista, R. K. Wang, P. Weinberg, and K. J. Ziegler, "Solvatochromic shifts of single-walled carbon nanotubes in nonpolar microenvironments," Phys. Chem. Chem. Phys. **12**, 6990 (2010).

[61] T. Hertel, A. Hagen, V. Talalaev, K. Arnold, F. Hennrich, M. Kappes, S. Rosenthal, James McBride, H. Ulbricht, and E. Flahaut, "Spectroscopy of Single- and Double-Wall Carbon Nanotubes in Different Environments," Nano Lett. **5**, 511 (2005).

[62] D. Bouilly, J. Cabana, F. Meunier, M. Desjardins-Carrière, F. Lapointe, P. Gagnon, F. L. Larouche, E. Adam, M. Paillet, and R. Martel, "Wall-Selective Probing of Double-Walled Carbon Nanotubes Using Covalent Functionalization," ACS Nano, **5** (6), 4927 (2011).

[63] S. Reich, C. Thomsen, J. Maultzsch, and P. Ordejon, "Tight-binding description of graphene," Phys. Rev. B **66**, 035412 (2002).

[64] M S. Dresselhaus, G. Dresselhaus, R. Saito, and A. Jorio, "Exciton Photophysics of Carbon Nanotubes," Annu. Rev. Phys. Chem. **58** 719 (2007).

[65] R.D. Mattuck, A Guide to Feynman Diagrams in the Many-Body problem, 2nd edn, (Dover, 1992).

[66] J. Jiang, R. Saito, G.G. Samsonidze, A. Jorio, S.G. Chou, G. Dresselhaus, and M.S. Dresselhaus, "Chirality dependence of exciton effects in single-wall carbon nanotubes: Tight-binding model," Phys. Rev. B **75**, 035407 (2007).

[67] V. Perebeinos, J. Tersoff, and P. Avouris, "Scaling of Excitons in Carbon Nanotubes," Phys. Rev. Lett. **92**, 257402 (2004).

[68] M. Rohlfing and S.G. Louie, "Electron-hole excitations and optical spectra from first principles," Phys. Rev. B **62**, 4927 (2000).

[69] E. Del Canto, K. Flavin, M. Natali, T. Perova, and S. Giordani, "Functionalization of single-walled carbon nanotubes with optically switchable spiropyrans," Carbon **48**, 2815 (2010).

[70] X. Zhou, T. Zifer, B.M. Wong, K. L. Krafcik, F. Leonard, and A. L. Vance, "Color Detection Using Chromophore-Nanotube Hybrid Devices," Nano Lett. 9, 1028 (2009).

[71] A. Hirsch and O. Vostrowsky, "Functionalization of Carbon Nanotubes," Top. Curr. Chem. **245**, 193 (2005).

[72] R. Khairutdinov, M. Itkis, and R. Haddon, "Light Modulation of Electronic Transitions in Semiconducting Single Wall Carbon Nanotubes," Nano Lett. **4**, 1529 (2004).

[73] X. Guo, L. Huang, S. OBrien, P. Kim, and C. Nuckolls, "Directing and Sensing Changes in Molecular Conformation on Individual Carbon Nanotube Field Effect Transistors," J. Am. Chem. Soc. **127**, 15045 (2005).

[74] M. Del Valle, R. Gutirrez, C. Tejedor, and G. Cuniberti, "Tuning the conductance of a molecular switch," Nature Nanotech. 2, 176 (2007).

[75] L. Cognet, D. A. Tsyboulski, J. R. Rocha, C. D. Doyle, J. M. Tour, and R. B. Weisman, "Stepwise Quenching of Exciton Fluorescence in Carbon Nanotubes by Single-Molecule Reactions," Science, **8**, 1465 (2007).

[76] J. G. Duque, A. N. Parra-Vasquez, N. Behabtu, M. J. Green, A. L. Higginbotham, B. K. Price, A. D. Leonard, H. K. Schmidt, B. Lounis, J. M. Tour, S. K. Doorn, L. Cognet, and M. Pasquali, "Diameter-Dependent Solubility of Single-Walled Carbon Nanotubes," ACS Nano **4**, 3063 (2010).

[77] T. Ando, "Environment Effects on Excitons in Semiconducting Carbon Nanotubes," J. Phys. Soc. Jpn. **79** , 024706, (2010).

[78] A. Nugraha, R. Saito, K. Sato, P. T. Araujo, A. Jorio, and, M. S. Dresselhaus, "Dielectric constant model for environmental effects on the exciton energies of single wall carbon nanotubes," Appl. Phys. Lett. **97**, 091905 (2010).

[79] R. Capaz, C. Spataru , S. Ismail-Beigi, and S. G. Louie, " Excitons in carbon nanotubes: Diameter and chirality trends," Phys. Stat. Sol. B **244**, 4016 (2007).

[80] S. Cambré, S. M. Santos, W. Wenseleers, A. R. T. Nugraha, R. Saito, L. Cognet, and B. Lounis, "Luminescence Properties of Individual Empty and Water-Filled Single-Walled Carbon Nanotubes," ACS Nano **6**, 2649 (2012).

[81] U. Hohenester and G. Goldoni, "Viewpoint: A new quasiparticle in carbon nanotubes," Physics bf 4, 5 (2011).

[82] Y. Tomio, H. Suzuura, and T. Ando, "Interwall screening and excitons in double-wall carbon nanotubes," Phys. Rev. B **85**, 085411 (2012).

[83] M. Rohlfing, "Redshift of Excitons in Carbon Nanotubes Caused by the Environment Polarizability," Phys. Rev. Lett. **108**, 087402 (2012).

[84] P. Finnie and J. Lefebvre, "Photoinduced Band Gap Shift and Deep Levels in Luminescent Carbon Nanotubes," ACS Nano **6**, 1702 (2012).

[85] R.S. Knox, *Theory of Excitons*, Solid State Physics Suppl. 5 (Academic Press, New York, 1963).

[86] H. Haken, *Quantum Field Theory of Solids: an Introduction* (New York, 1990).

[87] S. M. Bachilo, M. S. Strano, C. Kittrell, R. H. Hauge, R. E. Smalley, and R. B. Weisman, "Structure-Assigned Optical Spectra of Single-Walled Carbon Nanotubes," Science **298**, 2361 (2002).

[88] Y. Miyauchi, S. Chiashi, Y. Murakami, Y. Hayashida, and S. Maruyama, "Fluorescence spectroscopy of single-walled carbon nanotubes synthesized from alcohol," Chem. Phys. Lett. **387**, 198 (2004).

[89] H. Telg, J. Maultzsch, S. Reich, F. Hennrich, and C. Thomsen, "Chirality Distribution and Transition Energies of Carbon Nanotubes," Phys. Rev. Lett. **93**, 177401 (2004).

[90] V.L. Bonch-Bruevich and S.G. Kalashnikov, *Physics of Semiconductors* (Nauka, 1990).

[91] H. Haug and S.W. Koch, *Quantum Theory of the Optical and Electronic Properties of Semiconductors* (World Scientific, 2004).

[92] R. Saito, G. Dresselhaus, and M. S. Dresselhaus, "Trigonal warping effect of carbon nanotubes," Phys. Rev. B **61**, 2981 (2000).

[93] J. Deslippe, C. D. Spataru, D. Prendergast, and S. G. Louie, "Bound Excitons in Metallic Single-Walled Carbon Nanotubes," Nano Lett. **7**, 1626 (2007).

[94] E. Malic, J. Maultzsch, S. Reich, and A. Knorr, "Excitonic absorption spectra of metallic single-walled carbon nanotubes," Phys. Rev. B **82** 035433 (2010).

[95] M. F. Islam, D. E. Milkie, C. L. Kane, A.G. Yodh, and J.M. Kikkawa, "Direct Measurement of the Polarized Optical Absorption Cross Section of Single-Wall Carbon Nanotubes," Phys. Rev. Lett. **93**, 037404 (2004).

Vita

Personal Information

Born April 5th, 1982, Bamenda, North West Region, Cameroon

Education

2007 - 2012: PhD in Physics, Lehigh University, Bethlehem PA, USA
Thesis: Theoretical studies of the interaction of excitons with charged impurities in single-walled carbon nanotubes
Advisor: Slava V. Rotkin
2005 - 2007: M.Sc. in Condensed Matter Theory, University of Trieste, Italy
Thesis: One-dimensional electronic systems by Jastrow correlated wave function
Advisor: Sandro Sorella, SISSA, Trieste, Italy
2004 - 2005: Postgraduate studies, University of Buea, Cameroon
Referee: A. M. Dikande, University of Buea, Cameroon
2001 - 2004: B.Sc. (Hons) in Physics and Mathematics with a minor in computer sciences, University of Buea, Cameroon

Honors and awards

1) Abdus Salam ICTP-University of Trieste Joint Scholarship for Higher Education in Physics in 2005 - 2007.
2) Teaching assistantship award, Lehigh University, 2007.
3) Sherman Fairchild fellowship for solid state physics research, 2008 - 2010.
4) Research assistantship award, Lehigh University, 2008 - 2012.
5) Lehigh University student forum research grant, 2009.
6) College of arts and science (Lehigh university) travel support to 2010 APS March meeting.

Publications

1) Exact Jastrow-Slater wave function for the one-dimensional Luttinger model, Phys. Rev. B 78, 115117 (2008).
2) Charge impurity as a localization center for singlet excitons in single-walled carbon nanotubes (submitted).

Participant in international workshops/conferences

1) Miniworkshop on New States of Stable and Unstable Quantum matter, ICTP (Trieste), Italy, 2006.
2) School and Workshop on Highly Frustrated magnets and Strongly Correlated Systems: From Non-Perturbative Approaches to Experiments, ICTP (Trieste), Italy, 2007.
3) *Poster presentation*, 2009 Joint Annual Conference of the National Society of Black Physicists and the National Society of Hispanic Physicists, Nashville, TN (USA).
4) *Poster presentation*, 2009 APS March Meeting, Pittsburg, PA (USA).
5) *Poster presentation*, 2010 APS March meeting, Portland, OR (USA).
6) *Oral presentation*, 2011 APS March Meeting, Dallas, TX (USA).

Computer skills

1) Operating systems - GNU/Linux, Windows
2) Scientific - Mathematica
3) Content creation - LaTEX

Additional information

1) Currently writing a graduate level text book on the applications of quantum mechanics to atoms and molecules.
2) Taught mini course on quantum mechanics, Phy 369, spring 2010, Lehigh University.
3) Taught physics 22 for two semesters at Lehigh University.
4) Over four years of experience as a tutor, I tutored undergraduate and graduate students in the following areas: electrochemistry, physical chemistry, general physics, calculus, algebra, organic chemistry, thermodynamics, and business mathematics.